SAND2000-1800 J

Welding Behavior of Free Machining Stainless Steel

J. Brooks, C. Robino, T. Headley, and J. Michael
Sandia National Laboratories

Abstract

The weld solidification and cracking behavior of sulfur bearing free machining austenitic stainless steel was investigated for both gas-tungsten arc (GTA) and pulsed laser beam weld processes. The GTA weld solidification was consistent with those predicted with existing solidification diagrams and the cracking response was controlled primarily by solidification mode. The solidification behavior of the pulsed laser welds was complex, and often contained regions of primary ferrite and primary austenite solidification, although in all cases the welds were found to be completely austenite at room temperature. Electron backscattered diffraction (EBSD) pattern analysis indicated that the nature of the base metal at the time of solidification plays a primary role in initial solidification. The solid state transformation of austenite to ferrite at the fusion zone boundary, and ferrite to austenite on cooling may both be massive in nature. A range of alloy compositions that exhibited good resistance to solidification cracking and was compatible with both welding processes was identified. The compositional range is bounded by laser weldability at lower Cr_{eq}/Ni_{eq} ratios and by the GTA weldability at higher ratios. It was found with both processes that the limiting ratios were somewhat dependent upon sulfur content.

Introduction

The austenitic stainless steels with minor additions of sulfur, selenium, or lead can exhibit superior machinability with improved surface finishes, reduction in burring and higher cutting rates. These alloying elements form second phase particles which act as lubricants and enhance chip removal during the machining process. The most widely used free machining stainless steel is AISI 303, in which sulfur is used at levels as high as 0.4wt%. This level is an order of magnitude higher than the maximum allowable sulfur in AISI 304L of the same basic composition. Concerns regarding the affect of these high sulfur contents on weld fabrication and performance has limited the use of sulfur based stainless steels in applications involving welding.

It is recognized that sulfur can be extremely detrimental to weldability, especially in the formation of solidification hot cracks. However, Varestraint testing of 303 stainless steel by Lundin et al. (Ref. 1) indicated that high levels of sulfur can be tolerated without cracking if the weld solidifies as primary ferrite, while little sulfur can be tolerated if the weld solidifies as primary austenite. Brooks, et al. (Ref. 2) showed similar behavior in Fe-Ni-Cr ternary alloys with high levels of both sulfur and phosphorous. In conventional welding processes such as gas-tungsten arc (GTA) and shielded metal arc (SMA), the change in solidification mode from primary austenite to primary ferrite occurs at a Cr_{eq}/Ni_{eq} ratio of ~1.4 when using the equivalents of the WRC 92 diagram (Ref. 3). This ratio is ~1.50– 1.55 (Ref. 4-6) when using Hammar and Svennson equivalents (Ref. 7). For compositions with Cr_{eq}/Ni_{eq} ratios below these values, the welds typically solidify as primary austenite while above these values solidification occurs as primary ferrite. Other factors such as solidification velocity can, however, affect the solidification behavior.

Little data is available on high energy density (HED) welds of the free machining austenitic stainless steels. It is known that with the high solidification velocities common with these processes, the transition in solidification mode from primary ferrite to primary austenite occurs at

DISCLAIMER

higher Cr_{eq}/Ni_{eq} ratios than those given above, and this is due to dendrite tip undercooling (Refs. 8-20). Dendrite tip undercooling increases with increasing velocity for both ferrite and austenite, but the rate of this increase is greater for ferrite. Thus, a critical solidification velocity can exist above which the austenite phase will solidify at a higher temperature than that of ferrite and it therefore becomes the stable solidification phase. This critical velocity for transition from primary ferrite to primary austenite is dependent on composition (Ref. 13,15,19). In a manner similar to the more conventional welding processes, the role of solidification mode is very important in the weld cracking behavior during high energy density processing (at least with nominal levels of P and S (Ref. 21,22)). It must also be recognized that the solidification and solid state transformation behavior can be considerably different between the HED welding processes and the more conventional GTA and SMA welding processes (Refs. 10-12, 14, 16, 18, 20, 22).

In the manufacturing of engineering components it is common that several welding processes are used. One region of a component may require a GTA weld and another region a laser weld in the same material. In other cases, one heat of material or one material specification may be used for the manufacturing of a variety of components. Thus alloy compositions that exhibit good weldability for both processes would be very desirable. A goal of this investigation was to study the effect of sulfur content and solidification behavior on the weld cracking susceptibility of both GTA and pulsed YAG LBW in 303 type stainless steel, and to identify any differences which may exist between the two processes.

Experiments

Ten experimental heats were induction melted, cast, and hot rolled into strips ~ 7.6 cm wide and 3.2mm thick. Chromium and nickel contents were adjusted to provide a range of Cr_{eq}/Ni_{eq} ratios. Sulfur content was also varied while other minor alloying elements and impurities were held constant. The alloy compositions and heat designations are shown in Table 1. It can be seen that some of the materials are equivalent to 304L with high levels of sulfur, and others are characteristic to the 303 free machining grade with sulfur additions as high as 0.4%. Also shown in Table 1 are the Cr_{eq}/Ni_{eq} ratios calculated using the equivalents of both Hammar and Svennson and the WRC 92 diagram. However, for subsequent discussion the Hammar and. Svennson equivalents are used.

Sub-size Varestraint testing (Ref. 23) was used to determine the susceptibility to solidification cracking of the GTA welds. Composite samples were made by cutting 2.5 cm wide strips across the width of the alloy sheets and EB welding these to 304L end tabs. The composite specimens were 3.2 mm thick, 2.54 cm wide and 16.5 cm long. Weld parameters used for the Varestraint test were 90 amps, 12 volts, and 3 mm/sec travel speed with Ar shielding. Duplicate samples were run at augmented strains over a range of 0.5 to 3.6%. Crack lengths were measured at 30x magnification on the as-welded samples.

Autogeneous circular welds with a diameter of 1 cm were used to assess the cracking susceptibility of pulsed YAG laser welds. Two weld schedules were used, one at 20 Hz, 20 watts, and 3.4 mm/s (8 ipm) using 2.5 Joules/pulse and the other at 30 Hz, 75 watts and 4.6 mm/s (11 ipm) using 3.7 Joules/pulse. Single pulse weld cracking susceptibility was also conducted using a Weeter type test (Ref. 24) with a hole sizes of 0.483 mm in diameter ranging in depth from 0.203 to 0.508 mm.

Samples for metallographic examination were polished and etched with oxalic acid, and samples for transmission electron microscopy (TEM) analysis were thinned using a percloric acid polishing solution.

Electron backscattered diffraction (EBSD)was utilized to study the crystallographic orientation of individual grains in the weld metal. EBSD was performed in a JEOL 6400 scanning electron microscope (SEM) or a JEOL 5900LV SEM. Samples for EBSD were prepared by standard metallographic practice follwed by light electrolytic etching in oxalic acid or electropolishing in a perchloric acid solution. EBSD was conducted at an accelerating voltage of 20 kV with the a 70° sample tilt. It is possible to map the oreintation of many grains using EBSD. This was accomplished with the Noran Instruments Orkid system. Automated orientation mapping with EBSD is done by the automated acquisition and analysis of EBSD patterns for each pixel in an image. In this study the samples were scanned with grids of 200 x 200 pixels.

Results

GTA welds

The GTA weld Varestraint results are shown plotted as total crack length vs. augmented strain in Fig. 1. The crack length reported is the average of duplicate tests at each strain. It can be seen that there is a large range in cracking behavior. Heat 2 is seen to be by far the most susceptible to solidification cracking, while Heats 5 and 10 are extremely resistant to cracking (exhibited no cracking even at the highest strain of 3.6%). Table 2 shows the maximum crack length as a function of augmented strain for the same set of tests. It can be seen that at all strain levels the maximum crack length is greatest again for Heat 2 (Cr_{eq}/Ni_{eq} ratio of 1.95 and sulfur content of 0.039%). It can also be seen for Heats 1, 4, 6, 7, and 9 that the maximum crack lengths at the highest level of strain tested, 3.6%, are approximately the same. However, their cracking behavior at the lower strain levels is considerably different. The cracking response will be related to solidification mode and microstructure in a latter section.

The alloys can be separated into three groups to describe their solidification behavior. Alloys with a Cr_{eq}/Ni_{eq} ratio of 1.55 (Heats 1 and 7) generally solidified as primary ferrite (F/A) but did exhibit some regions of primary austenite solidification with small amounts of eutectic ferrite (A/F). Figure 2(a) shows the overall solidification structure and cracking behavior of Heat 7 (0.11% S). The darker etching regions which are located primarily near the weld centerline solidified as primary austenite, and the lighter etching regions as primary ferrite. The higher magnification micrograph in Fig. 2(b) shows cracks in the primary austenite solidified region. The dark etching spherical particles were identified as sulfides and are primarily located in the interdendritic regions of the structure. The cracking behavior of Heat 1 (with the same Cr_{eq}/Ni_{eq} ratio as Heat 7, but a lower sulfur content of 0.039%), is shown in Fig 3(a). This weld generally solidified as primary ferrite, but many of the grain boundary regions solidified as austenite as shown at higher magnification in Fig 3(b). This microstructure and cracking behavior was similar in Heats 7 and 1 in the regions of F/A solidification. An SEM micrograph of the region ahead of the crack in Heat 7 is shown in Fig 3(c). The cracks are present along austenite solidification grain boundaries, and are associated with sulfides. The small spherical sulfides segregated at the cell boundaries and ahead of a crack tip (some of which have been etched away during metallographic preparation) are clearly visible in Fig. 3(c). It was found by SEM EDS analysis that the sulfides contain Mn and Cr. Some eutectic ferrite is also apparent in Fig. 3(c). It appears that the regions local to the grain boundaries were sufficiently modified in composition by segregation and/or back filling with Ni enriched liquid during Varestraint testing to result in austenitic solidification with eutectic ferrite (A/F).

The second group of alloys is those with a Cr_{eq}/Ni_{eq} ratio in the range of 1.73-1.85 (Heats 3, 8, 9 and 10). These alloys solidified as primary ferrite and exhibited a skeletal ferrite morphology with some regions of lathy ferrite. An example of this microstructure is shown in Fig. 4(a) for Heat 10 with a Cr_{eq}/Ni_{eq} ratio of ~1.85, tested at a strain of 1%. This heat did not crack at any strain level tested. The micrograph was taken near the trailing edge of the weld pool where cracking would be expected in the Varestraint test. The different etching behavior of the grain boundary regions is a result of highly localized strain and possibly backfilling during testing. One such region is shown at higher magnification in the SEM image of Fig. 4(b). A large concentration of sulfide particles are evident at the ferrite / austenite boundaries, in the solidification cell boundaries, and especially in the grain boundary regions which exhibited the different etching behavior.

The third group of alloys is those with Cr_{eq}/Ni_{eq} ratios in the range of 1.92 to 1.95. The microstructure of Heat 2 (Cr_{eq}/Ni_{eq} ratio ~1.95) shown in Fig. 5(a) is typical of this group of welds. This microstructure is characteristic of welds that solidify completely as ferrite and the transformation to austenite occurs at a temperature considerably below that of final solidification (Refs. 9, 25, 26). In this case the ferrite exhibits a more lath-type structure in which the laths can extend across a number of solidification cell diameters thereby masking the cell boundaries. The grain boundary crack shown in the micrograph is typical of alloys in this group and occurred when tested at an augmented strain of 2.5%. At higher magnification, Fig. 5(b), the grain boundary regions are more apparent and are seen to contain little ferrite and a large concentration of sulfides (even at the low sulfur level of 0.039%). Although this heat has one of the lowest levels of sulfur, it exhibited the most severe cracking of all the heats studied.

Laser welds

The cracking behavior of laser welds made with both weld schedules was assessed by metallographically examining cross-sections every 90 degrees in the circular welds. It was found that the two heats with a Cr_{eq}/Ni_{eq} ratio of ~1.55 (Heats 1 and 7) exhibited severe cracking. The sulfur contents of these heats are 0.04 and 0.11%. Heat 9 (Cr_{eq}/Ni_{eq} ratio ~1.74, sulfur level = 0.27%) was the only other heat to exhibit cracking in these tests, and the cracking was much less severe than in Heats 1 and 7. The other two heats with the same Cr_{eq}/Ni_{eq} ratios similar to Heat 9 but lower levels of sulfur, 0.04% and 0.12%, did not exhibit cracking. Cracking was not observed at any sulfur level in the heats with the highest Cr_{eq}/Ni_{eq} ratios of 1.85 to 1.95.

The cracking behavior of all the laser welds are plotted in Fig. 6 for different impurity levels (P+S) and Cr_{eq}/Ni_{eq} ratios. Also shown are results of Pacary et al. (Refs. 21,22) for 304L stainless steel. The justification for plotting the results in terms of combined phosphorus and sulfur level is based more on convention than on experimental data (Refs. 5, 27-29). It is recognized that both elements can form low melting liquids that can lead to solidification cracks, but the potency of each element may well be different. It was found in GTA welds of Fe-Ni- Cr ternary alloys that phosphorous was more detrimental to solidification cracking response than sulfur (Refs. 2,9). This difference was related to the nature of the eutectic liquids, i.e. phosphides formed films that more readily wet the solidifying boundaries while sulfides tended to form as spherical droplets. The effect of these two elements on both HAZ and solidification cracking is still an area of active research (Ref. 30). Since the goal of the work was to determine the effect of sulfur level, the phosphorus level was kept constant and near the upper extreme of typical austenitic stainless steel specifications. In this way the results should represent worst case behavior, but it must be recognized that phosphorous may be influencing the cracking behavior. The narrow line in the diagram of Fig. 6 which separates regions of cracking and no cracking is that determined by Pacary et.al (Ref. 21) for alloys with lower levels of phosphorous and sulfur. The heavier line in Fig. 6 at higher Cr_{eq}/Ni_{eq} represents the behavior of the two combined studies. However, it can be seen that only one data point generated here separates the results and that more data is needed at the higher sulfur levels. It should also be noted that in the data for GTA welds, there are heats that were classified as crack susceptible at higher Cr_{eq}/N_{eq} ratios than the value of ~1.5 separating "cracking" from "no cracking" (Refs. 5,31). Thus, it is not surprising that the laser welds would exhibit similar behavior, and that one finite Cr_{eq}/Ni_{eq} ratio cannot clearly separate all weld cracking results. (last two sentences need rewording)

The laser welds were evaluated using light microscopy, scanning electron microscopy (SEM), and TEM techniques. All the welds consisted of single-phase austenite with no detectable ferrite.

Although the laser weld solidification behavior and microstructures were considerably different from the GTA welds, in general they can also be separated into three groups based on Cr_{eq}/Ni_{eq} ratio. The alloys with a Cr_{eq}/Ni_{eq} ratio of 1.55 (Heats 1 and 7) solidified completely as austenite. The austenite solidification structure and severe cracking behavior of Heat 7 with 0.11 sulfur is shown in the low magnification micrograph in Fig. 7(a). The higher magnification image of Fig. 7(b) shows the very distinct cellular solidification structure typical of primary austenite, with weld cracks confined to the austenite grain boundaries. It is interesting to note that the grain size appears smaller than is apparent at the lower magnification.

A STEM image from a weld in Heat 1, Cr_{eq}/Ni_{eq} ratio of 1.55, which contains 0.04% sulfur is shown in Fig. 8. In this micrograph the cellular solidification structure resulting from microsegregation is also very evident. However, the degree of microsegregation was small with a measured cell boundary enrichment in Cr and Ni of only ~1wt %. The particles noted with the arrows marked with "O" are amorphous Al containing oxides and the particles with marked "P" are Cr containing phosphides. However, no sulfides were observed in the cell boundaries of TEM samples at this sulfur level (0.04%).

Regions of cracking were examined compositionally in Heat 7 using energy dispersive spectrometry and spectrum imaging. Spectrum imaging is the collection of a full EDS x-ray spectrum at each pixel in an image. Once the maps are collected it is possible to form chemical images. A SEM image of a region analyzed is shown in Fig. 9(a) while the maps of phosphorous and sulfur are shown in Fig.9(b) and (c). It is apparent that the phase associated with the crack is enriched in both these elements.

The second group of alloys are those with Cr_{eq}/Ni_{eq} ratios of ~1.74. In general the solidification behavior of these alloys was different than those with lower Cr_{eq}/Ni_{eq} ratios, with the exception of Heat 9 which contained a higher level of S, 0.27%. The majority of the weld in Heat 9 also solidified as primary austenite, as did the two heats with the Cr_{eq}/Ni_{eq} ratio of 1.55. An example of the microstructure showing the characteristic austenite solidified cellular dendritic structure is shown in Fig 10(a) and at higher magnification in Fig 10(b) along with several small intergranular solidification cracks. The fine grain structure is again apparent. The Weeter test results on this heat were similar to the circular welds, and showed that it was relatively resistant to cracking, although a few small cracks were observed as shown in Fig. 10(c). This sample was etched more lightly than the sample in 10(b) and clearly shows the solidification crack along on austenite grain boundary. Also apparent are darker etching grain boundaries that contain large quantities of sulfides.

The weld microstructures of the other two heats with a Cr_{eq}/Ni_{eq} ratio of 1.74 exhibited a different appearance. A representative microstructure is shown in Fig. 11(a) for Heat 3 with 0.04% sulfur. These welds contain isolated grains (primarily at the fusion line and interpass boundaries) that exhibit the same cellular solidification structure as the laser welds in the low Cr_{eq}/Ni_{eq} ratio heats. However, the majority of the weld is composed of grains that exhibit little or no evidence of a solidification structure. Such a region is shown at higher magnification in Fig 11(b). It was concluded, as have other workers (Ref. 22), that grains that exhibited little segregation solidified as ferrite while grains or regions that clearly exhibited microsegregation or well pronounced solidification cells solidified as austenite. The rationale for this is discussed in more detail below.

The third group of alloys (with Cr_{eq}/Ni_{eq} ratios of ~1.85 to 1.95) solidified totally as ferrite and again contained no detectable residual ferrite in the optical microscope, SEM or TEM. The microstructure of Heat 2 (Cr_{eq}/Ni_{eq} = 1.95, S=0.04%) is shown at low magnification in Fig. 12(a) and the overlapping laser pulses are clearly visible. The boundary regions are shown at higher magnification in Fig. 12(b) along with ferrite stringers in the base material. The weld microstructure of an alloy with a similarly high Cr_{eq}/Ni_{eq} ratio, but with high S content (Heat 6, S= 0.42), is shown in Fig 13(a). The low magnification micrograph appears very similar to that a

shown in Fig 12A, except that it is much darker due to the high concentration of sulfides. The fusion zone boundary region is shown at higher magnification in Fig 13(b). In this micrograph the sulfides are visible as spherical particles in the fusion zone, as large globules at the fusion zone boundary, and as stringers (darker etching) in the base material. Laser welds of the alloys with the high Cr_{eq}/Ni_{eq} ratios were also studied in TEM. In samples with the lower sulfur levels, 0.04 wt%, no sulfides were observed although some spherical oxides similar to those in Fig. 8 were noted. In the alloy that contained the highest sulfur content, Heat 6, sulfides exhibit a bimodal distribution of sub-micron size particles as shown in the TEM micrograph in Fig 13(c). Many of the larger particles in the solidified structure are comprised of amorphous aluminum oxide surrounded by Cr and Mn containing sulfides. The largest particles are contained in the solidification cell boundaries, although many of the particles are also present within the columnar dendritic structure. The smaller spherical sulfides noted in Fig 13c are more uniformly distributed throughout the structure. It is likely that these particles, ~200 angstroms in diameter, precipitated from the solid state during weld cooling. These smaller sulfides also contained primarily Mn and Cr. It is interesting to note that even with this high sulfide content, cracks were not observed in the weld structure.

The austenitic stainless steels are complicated by the transformation of austenite to ferrite at high temperature. Thus, in GTA welds that solidify as ferrite, a region of the HAZ from which solidification occurs can be ferrite that formed on heating, which then transforms back to austenite during cooling. Experimental evidence of this transformation has been observed during Gleeble testing (Ref. 23), liquid tin weld quenching (Ref. 26), as well as in as solidified weld structures (Ref. 32). The formation of HAZ ferrite has also been observed insitu using x-ray diffraction techniques (Ref. 33). It is not clear with the high heating rates of pulsed laser welds if, or to what extent, a transformation to ferrite occurs in the higher Cr_{eq}/Ni_{eq} ratio alloys prior to solidification. However, the crystal structure at the fusion zone boundary at the time of solidification could have a major effect of the overall weld solidification behavior, especially on the mixed mode solidification behavior apparent at the intermediate Cr_{eq}/Ni_{eq} ratios. To study this in more detail electron backscattered diffraction (EBSD) analysis (Ref. 34) was used for both phase identification and to determine relative crystallographic orientations.

A number of fusion zone boundary regions were studied in Heat 3 (Cr_{eq}/Ni_{eq} ratio ~1.74). As shown in Fig 11, a mix in solidification mode of ferrite and austenite was most apparent at this Cr_{eq}/Ni_{eq} ratio. First, different regions were examined, some with grains that exhibited a highly cellular structure (primary austenite) and others with grains which exhibited little segregation effects (primary ferrite). It was found in all cases that both solidified structures were indeed face-centered cubic (FCC) with no detectable regions of ferrite. This observation is consistent with the TEM results. It was also found that grains exhibiting the distinct cellular structure exhibited the same crystallographic orientation as the grain from which they grew, supporting the hypothesis that epitaxial growth of austenite from austenite had occurred. Moreover, similar behavior was observed at both base metal and interpulse fusion lines. An example at an interpulse boundary where the austenite diffraction patterns are the same in both regions is shown in Fig14. Regions were also examined where a cellular solidification region grew for a short distance before leading into a more featureless (ferrite solidified) structure. Such a region is apparent in Fig 15 in which the cellular structure again has the same orientation as the base grain. However, the featureless region only a few microns away has a different orientation, although microstructurally it appears to be within the same grain. The apparent growth of ferrite directly from the base grain in which the base grain and solidified region have different austenite orientations is shown in Fig. 16.

In a similar manner, orientation maps were used to examine a large region of the fusion zone boundary. An example of primary austenite solidification is shown in Fig. 17 for a weld in Heat 1. An SEM image of a region analyzed is shown in 17(a) where the sample is tilted 70° to obtain the Kikuchi patterns. The corresponding orientation map is shown in Fig. 17(b) where the grains are colored coded according to their orientation. Due to epitaxial growth it is impossible from the map alone to determine the fusion zone boundary. The ferrite solidified welds are, however, much different. Fig. 18 shows an SEM image and corresponding orientation imaging map of a weld in Heat 4 with a Cr_{eq}/Ni_{eq} ratio of 1.95. In this map the region of the fusion zone boundary is much more apparent due to the differences in grain orientation. Considerably more grains are apparent on the fusion zone side of the boundary with relatively few cases where a single substrate grain corresponds to a single fusion zone grain. Thus it appears that in the case of ferrite solidification, the nucleation and growth conditions are more complex, but consistent with the differences in microsegregation behavior. However, the mechanics of initial ferrite solidification is difficult to assess due to the transformation to austenite on cooling.

Discussion

GTA welds

It has been well established in conventional welds, such as GTA, that a strong correlation exists between solidification mode and weld cracking (Refs. 5, 9, 31, 35-38). Welds that solidify as primary ferrite with the secondary solidification of austenite, and welds which solidify totally as ferrite in which the transformation to austenite starts at a temperature near the solidus are extremely resistant to solidification cracking. Welds that solidify as austenite are very susceptible to cracking, although this susceptibility can be significantly reduced at low phosphoropus and sulfur impurity levels. The transition in solidification mode from primary austenite to primary ferrite in low speed GTA welds occurs at a Cr_{eq}/Ni_{eq} ratio ~1.5-1.55 when using Hammar and Svennson equivalents (Ref. 5) (~1.4 when using the WRC diagram). Similarly, welds that solidify totally as ferrite with a lower transformation temperature to austenite are also susceptible to cracking, although this behavior is not as well documented. This tendency for cracking at high Cr_{eq}/Ni_{eq} ratios has been reported by Kajampaa et al. (Ref. 31) to occur at Creq/Nieq ratios above ~ 2.1.

In examining the Varestraint data in Fig. 1 it can be seen that the heat most susceptible to weld cracking is Heat 2 with the highest Cr_{eq}/Ni_{eq} ratio, 1.95, and the lowest sulfur content, 0.04 wt%. The next most susceptible heats, 1, 7, and 4 all exhibited similar cracking behavior. Heats 1 and 7 both have a Cr_{eq}/Ni_{eq} ratio of 1.55 and sulfur levels of 0.04 and 0.11%, respectively, and exhibited almost identical cracking behavior. The third heat of this group, Heat 4, had a slightly higher cracking response, a Cr_{eq}/Ni_{eq} ratio of 1.92 and a sulfur level of 0.11 wt%. The two heats that exhibited no cracking at any strain level were Heats 5 and 10 with Cr_{eq}/Ni_{eq} ratios of 1.94 and 1.85 and sulfur levels of 0.27 and 0.18 wt%, respectively. The overall GTA Varestraint cracking behavior is summarized in Fig. 19 and plotted as (S+P) content vs. Cr_{eq}/Ni_{eq} ratio. In general, it can be seen that the data can be bound with a lower limit somewhat above 1.55 and a higher limit at ~ 1.9. However, it was observed that the heats with the Cr_{eq}/Ni_{eq} ratio ~1.55 contained some regions solidified as austenite, primarily near the weld centerline, e.g. Fig. 3, Heat 7 with 0.11 wt% sulfur. These regions were very susceptible to cracking. The transition in solidification from primary ferrite to primary austenite near the weld centerline has been reported previously in both GTA (Ref. 39) and EB processes (Ref. 38), and has been attributed to differences in dendrite tip velocity. In that work it was thought that the solidification velocity was higher near the weld centerline; sufficiently high to exceed the critical dendrite tip velocity for the change in mode from primary ferrite to primary austenite. This type of behavior will typically occur at compositions near the critical Cr_{eq}/Ni_{eq} ratio of 1.55, and is likely the cause of the change in solidification mode observed here. However, it was also observed that in primary ferrite solidification regions of welds with the Cr_{eq}/Ni_{eq} ratio ~1.55 relatively severe cracking also occurred. This is somewhat surprising and may be due to the formation of high quantities of low melting liquids at the grain boundaries during the final stages of the secondary (peritectic) solidification of austenite. It may be at this high level of impurities, slightly higher Cr_{eq}/Ni_{eq} ratios, with a concomitant larger fraction of ferrite solidification, are required to significantly reduce cracking. It is further possible that high levels of sulfur promote austenite solidification and is also responsible for differences in solidification behavior of the two heats with the Cr_{eq}/Ni_{eq} ratio ~1.55. For example, it has been observed that in Fe-Ni-Cr ternary alloys at Cr/Ni ratios as high as ~1.6, high levels of sulfur tended to promote austenite solidification and alter residual ferrite content (Ref. 39). In that study it was suggested that sulfur (in the absence of Mn) effectively reduced the Cr equivalent by forming CrS. However, in the current work it was found that although the sulfides contained Cr, they also contained high concentrations of manganese (which would tend to reduce the nickel equivalent and thereby offset the reduction in chromium equivalent).

Fig. 19 summarizes the GTA Varestraint test results in terms of composition (e.g Cr_{eq}/Ni_{eq} ratio and impurity level). As shown, at intermediate Cr_{eq}/Ni_{eq} ratios the alloys are resistant to relatively high impurity levels. The upper and lower bounds of the low susceptibility region are consistent with the work of Suutula and Kujanpaa (Ref. 31), although the limits are somewhat tightened, 1.55 to 1.9, compared to their values of 1.5 to 2.1 (using Hammar & Svennson equivalents). The value of 1.55 is well within the data they compiled, especially at high levels of phosphorous and sulfur, while the value of 1.9 vs. 2.1 may be related to weld test techniques. Since the change in cracking behavior is not associated simply with an abrupt change in solidification mode, as is the case of the lower bound of Cr_{eq}/Ni_{eq} ratio, it would be expected that the upper limit might not be as well defined. However, the change in cracking behavior is still related to solidification and solid state transformation behavior. It is clear from the microstructures of the heats with Cr_{eq}/Ni_{eq} ratio of ~1.94, with the ferrite extending over a number of cell boundaries (Fig 5(a),that the welds solidified completely as ferrite. Moreover, the morphology of the ferrite suggests that the transformation of ferrite occurred at a temperature considerably below the solidus temperature (Refs. 9. 25, 26). The rationale summarized (Ref. 2,9) to explain cracking behavior is consistent with the GTA weld data shown here. Solidification crack initiation and propagation along the complex interphase boundaries formed during ferrite-austenite solidification, or that result from high temperature transformation of primary ferrite to austenite, is more difficult than along the rather smooth single phase grain boundaries (Ref. 40). These single phase boundaries occur at both the low Cr_{eq}/Ni_{eq} ratios with austenite solidification, and at high Cr_{eq}/Ni_{eq} ratio where single phase ferrite solidification predominates. Also, crack propagation is more difficult along the lower surface energy δ–γ boundaries than along the higher energy γ–γ and δ–δ boundaries (Ref.41).

The upper bound Cr_{eq}/Ni_{eq} ratio of ~1.9 for favorable cracking resistance appears to be dependent upon S sulfur content; i.e. the higher the sulfur level at a Cr_{eq}/Ni_{eq} ratio of ~1.93, the greater the resistance to cracking. This behavior was also observed in ternary heats doped with high levels of sulfur (Ref. 2) and may be the result of backfilling from sulfur containing eutectic liquid. In Fig. 3 it appears from the etching behavior that the grain boundary regions (which did not form cracks) underwent considerable strain and contain large amounts of sulfides. These observations are consistent with a backfilling mechanism.

It has been suggested that the maximum crack length at the saturation strain level may be a better indicator of cracking behavior than the total crack length plotted against augmented strain. When analyzing Varestraint data the saturation crack length at the highest strains corresponds to the temperature sensitive region for cracking. The length of this region in a given weld is then directly related to the thermal gradient along the weld centerline, for a centerline crack, and the weld speed. The highest strain tested, 3.6%, may be close to the saturation strain. If this is the case, the maximum crack lengths at 3.6% strain in Table 2 would suggest Heat 2 is the most susceptible heat and this agrees with the total crack length data of Fig 1. However, based on maximum crack length, the cracking behavior of Heats 4, 6, 7,and 9 should all be very similar and likely not that different from Heats 1 and 2. We believe that the results in Figs. 1 and 19, rather than the maximum crack length at 3.6% strain, may be more representative of cracking response in production environments for the heats of material studied here.

Laser welds

Before discussing the solidification cracking behavior of the laser welds, or correlating solidification cracking behavior to solidification mode, one must be able to distinguish between the two primary modes of solidification. In the welds studied here, the primary microstructural features used to distinguish solidification mode were differences in the degree of microsegregation and differences in cellular appearance in the optical and electron microscopes. In all the laser welds studied, no ferrite was observed which could be used to help more clearly define solidification behavior. We concluded, as have others (Ref. 22), that the weld regions that exhibited the distinct cellular dendritic structure solidified as primary austenite while those regions that exhibited little or no evidence of the cellular solidification structure solidified as ferrite. These conclusions were based on earlier studies that showed that the combined effect of dendrite tip undercooling and solid state diffusion is much more effective in reducing microsegregation during ferrite solidification than in austenite solidification. However, other workers have proposed that partitionless solidification occurs during primary ferrite solidification of high energy density laser welds (Ref. 13). The use of EBSD further supported the relationship between solidification mode and the degree of microsegregation. In all cases studied, it was found that the crystallographic orientations of the weld and substrate were the same for regions of austenite solidification and were consistent with epitaxial growth. However, the orientations of the substrate grain and primary ferrite solidified, low segregation regions were different, indicating the initial stages of solidification are different.

It has been suggested (Ref. 22) that for pulsed laser welds of compositions similar to those of this study, initial solidification occurs epitaxially as austenite; the diffusion controlled transformation kinetics for ferrite formation may be too slow at the rapid heating rates. The mode of further solidification is then dependent upon dendrite tip velocity. Since growth occurs along the <100> directions, dendrite tip velocities will depend on the orientation of the individual grains relative to that of the solidification front and maximum thermal gradient. It is further suggested that, when the solidification velocity is close to the transitional velocity for a specific composition, the range in solidification velocities resulting from these geometric constraints may be sufficient to result in mixed mode solidification (as was also seen in the GTA welds discussed above). For the laser welds, this is applicable to the compositions with Cr_{eq}/Ni_{eq} ~1.7. However, it has also been shown that the change in solidification mode from austenite to ferrite may involve a nucleation barrier that does not exist in the transition in solidification from ferrite to austenite (Ref. 15). Thus dendrite tip undercooling resulting from small changes in velocity due to orientation differences may be insignificant compared to the undercooling needed to overcome the barrier to nucleation of ferrite. The EBSD work here suggests that the nature of the substrate may be playing a major role on the solidification behavior. Furthermore, the kinetics of a massive transformation of austenite to ferrite may be sufficiently fast for transformations at the HAZ to occur. It appeared in some cases that a single grain of ferrite solidified from a single substrate grain, Fig. 16. This observation suggests that the FZ boundary region was ferrite at the time of initial solidification, possibly as a result of a massive transformation. It would seem that if ferrite nucleated at an austenite interface, numerous grains may be coincident with individual substrate grain, unless ferrite nucleated on the austenite with a preferred, low energy, orientation. The EBSD patterns in Fig 17(b) covering a large region of the weld show that the FZ boundary region consists of more grains than that of the corresponding substrate. However, in this heat with a higher Cr_{eq}/Ni_{eq} ratio (1.95), the solidified ferrite massively transforms to austenite, yielding a finer grain structure and further complicating the solidification behavior. Thus initial solidification of ferrite in the pulsed laser welds appears complex and is being further studied. Nevertheless, the use of segregation patterns to distinguish solidification mode, which is important for this study, is consistent with the crystallographic orientations observed for the different structures.

Irrespective of the details of the solidification mechanics, it was found that only welds that solidified as primary austenite exhibited weld cracking. This behavior is consistent with earlier results on pulsed laser welds with lower levels of phosphorous and sulfur (Refs. 21, 22). The current data is also consistent with previous work which indicates that that the change in solidification mode due to dendrite tip undercooling occurs at a Cr_{eq}/Ni_{eq} ratio of about 1.68. However, we found that with a Cr_{eq}/Ni_{eq} ratio of 1.74 the welds still solidified in a mixed mode, although the fraction of primary ferrite solidification was typically high, ~75% or greater. An exception was Heat 9 with the highest amount of sulfur (0.27), in which a large fraction of the weld solidified as primary austenite. In this heat however, only a small amount of cracking was observed. In the Weeter tests of this heat the solidified grain boundaries contained large amounts of sulfides, which implies that sufficient euctectic liquid was available to heal or prevent the formation of cracks in a manner similar to the GTA welds in Heat 6. It is not clear why the solidification behavior of Heat 9 is different than the other heats with the same Cr_{eq}/Ni_{eq} ratio. The reduction in Cr by the formation of sulfides within the melt would be small due to the high concentration of Mn in the (Mn, Cr)S (this behavior is also similar to that observed in the GTA welds of Heat 7 with a higher sulfur content than Heat 1). However, it should be noted that similar discrepancies in solidification mode at constant Cr_{eq}/Ni_{eq} ratios were also observed in another study involving austenitic stainless steels and electron beam welds (Ref. 19), although in the current study the basic compositions are almost identical except for sulfur.

In light of the GTA Varestraint test results, it is interesting to note that the laser welds with the highest Cr_{eq}/Ni_{eq} ratios seemed resistant to cracking. This lack of cracking is inconsistent with the hypothesis that cracking susceptibility is high for single-phase ferrite solidification when the transformation to austenite occurs at lower temperatures, as it would for a massive transformation. It was evident that even though the solubility of sulfur is higher in ferrite than in austenite, a large amount of sulfides still formed during solidification. Since no cracking was observed at any level of sulfur tested, a simple eutectic healing mechanism can not be invoked.

In one of the heats with the lowest Cr_{eq}/Ni_{eq} ratio that solidified as austenite and exhibited extensive cracking (Heat 7), it was found that low melting phases associated with the cracks contained both sulfur and phosphorus, Fig. 9. The sulfur content of this heat was 0.11%. However, sulfides were not observed in TEM in the austenite solidified welds of Heat 1with the lower sulfur level which still exhibited severe cracking. Thus, it is conceivable that phosphorus is primarily responsible for cracking and not sulfur. The phosphorus content of all the heats was relatively high, 0.03%. Given the higher phosphorus solubility in ferrite than austenite, higher levels of phosphorus may be tolerated in those heats solidifying as ferrite.

The results of the GTA and laser welding trials can be combined to describe alloy compositions which are amenable to welding with either conventional or HED processes. This combination is shown in the summary plot of Fig. 20. As shown, a lower weldability limit occurs at a Cr_{eq}/Ni_{eq} ratio of ~1.7 and is established by the laser weld process, while the upper weldability limit of ~ 1.9 is established by the GTA process. The boundaries at these limits are sloped, which implies that the limits are somewhat dependent upon sulfur content, although additional data is desirable. As discussed earlier, it is important to emphasize that although the data is portrayed in terms of total impurity level (P+S), it should be remembered that this portrayal is based more on convention than a strong experimental or theoretical basis. Nevertheless, Fig. 20 illustrates that reasonable fabrication weldability can probably be achieved in free machining grades through suitable choice of alloy composition. Future work will describe the mechanical properties of welds in these types of alloys.

Summary

A study was conducted to determine the solidification behavior and cracking response of high sulfur austenitic stainless when welded with both the GTA and pulsed YAG laser weld processes. Experimental heats with a wide range in Cr_{eq}/Ni_{eq} ratios and sulfur contents were evaluated. The heats also contained high levels of phosphorus, 0.03 wt%. GTA weld solidification modes were consistent with those predicted with existing diagrams. The cracking response was controlled primarily by solidification mode. When using Suutula equivalents, the lower bound of Cr_{eq}/Ni_{eq} ratios for good cracking resistant was ~1.55, while the upper bound was ~1.9. This response is consistent with existing rationale for describing solidification cracking behavior of austenitic stainless steels. However, at the upper limit, high sulfur appeared to reduce the cracking susceptibility of the single-phase ferrite solidified welds and this reduction was attributed to eutectic healing involving sulfur-containing liquid. The exact role of sulfur appears to be complex and may affect solidification mode.

The solidification behavior of pulsed laser welds was also generally related to Cr_{eq}/Ni_{eq} ratio. However, solidification in the laser welds is complex, and in many cases the welds exhibited mixed mode solidification behavior. As with the GTA welds, the solidification cracking behavior of the laser welds was related to solidification mode. At Cr_{eq}/Ni_{eq} ratios of 1.55 welds solidified as austenite and were susceptible to cracking. Welds in alloys with Cr_{eq}/Ni_{eq} ratios of 1.74 solidified in a mixed mode, with some regions solidifying as ferrite and other regions as austenite, but in general appeared to exhibit good cracking resistance. However, with the same Cr_{eq}/Ni_{eq} ratio but a higher level of sulfur, 0.27%, the amount of austenite solidification increased, and a small amount of cracking was observed. At the Cr_{eq}/Ni_{eq} ratios of 1.92 the welds solidified completely as ferrite, but unlike the GTA welds the resistance to cracking was high at all impurity contents. In the laser welds phosphorus is likely to be playing a major role in weld cracking behavior. For the alloys studied, good cracking resistance was observed within a range of Cr_{eq}/Ni_{eq} ratios of ~1.7 to 1.9, with the lower limit established by the laser process, and the upper limit established by the GTA cracking behavior.

Acknowledgements

Special thanks is given to Andy Gardea for metallographic services and to Annette Newman for laboratory support on weldability testing. Thanks are also given to Mike Cieslak for reviewing the manuscript. The experimental alloys were produced by Carpenter Technology Corporation, and their participation is greatly appreciated. Sandia is a multiprogram laboratory operated by Sandia corporation, a Lockheed Martin Company, for the United States Department on Energy under Contract DE-AC04-94AL85000.

References

1. Lundin, C. D. Lee C. H., and Menon, R. 1988. Hot ductility and weldability of free machining austenitic stainless steel. *Welding Journal*, 67, (6): 122-s to 130-s.

2 Brooks, J. A., Thompson, A. W. and Williams, J. C. 1984. A fundamental study of the beneficial effect of delta ferrite in reducing weld cracking, *Welding Journal* 63 (2): 71-s to 83-s.

3. Kotecki, D. and Siewert, T. A. 1992. WRC-1992 constitution diagram for stainless steel weld metals: a modification to the WRC-1988 diagram. *Welding Journal* 71(5): 171-s to 179-s.

4. Suutula, N. 1982. Effect of solidification conditions on the solidification mode in austenitic stainless steels. *Acta Universitatis Ouluensis, Sreries C Technica* No. 23, University of Oulu,Oulu, Finland.

5. Takalo, T., Suutula, N. and Moisio, T. 1979. *Metall. Trans* , 10A(4), 1173-1181.

6. Olsen. D. L., 1985. Prediction of austenitic weld metal microstructure and properties. *Welding Journal* 64 (11):181-s to 295-s.

7. Hammar, O. and Svensson, U. 1979. Influence of steel composition on segregation and microstructure during solidification of austenitic stainless steels, *Solidification and Casting of Metals*, The Metals Society, London: 401-410.

8. Kurz, W. and Fisher, D. J. 1989. *Fundamentals of Solidification*, Trans Tech Publications Ltd. Switzerland.

9. Brooks, J. A. and Thompson, A. W. 1991. Microstructural development and solidification cracking susceptibility of austenitic stainless steel welds. *International Materials Reviews* 36 (1): 16-44.

10. David S. A. and Vitek J. M. 1981. Solidification behavior and microstructural analysis of austenitic stainless steel laser welds. in *Lasers in Metallurgy*, K. Mukherjee and J. Mazumder, eds., TMS-AIME, Warrendale, PA: 247-254.

11. Vitek, J. M., Dasgupta, A., and David, S. A. 1983. Microstructural modification of austenitic stainless steels by rapid solidification. *Metall. Trans A* 14A: 1833-1841.

12. Katayama, S. and Matsunawa, A. Proc. *ICALEO*, San Francisco, 1985.

13. Elmer, J. W. 1992. Non-equilibrium microstructures produced during electron-beam and laser-beam surface modification of metallic alloys, *The Metals Science of Joining*, ed Cieslak, Perepezko, Kang and Glicksman, TMS, Warrendale PA: 123-133.

14. Brooks, J. A., Baskes, M. I. and Greulich, F. A. 1991. Solidification modeling and solid state transformations in high energy density welds. *Metall. Trans.* 22A: 915-925.

15. Fukumoto, S. and Kurz, W. 1997. The δ–γ transition in Fe-Cr-Ni alloys during laser treatment, *ISIJ International*, 37 (7): 677-684.

16. Elmer, J. W., Allen, S. M., and Eagar, T. W. 1989.Microstructural development during solidification of stainless steel alloys. *Metall. Trans* 20A: 2117-2131.

17. David, S.A., Vitek, J. M. and Hubble, T. L. 1987. Effect of rapid solidification on stainless steel microstructures and its implication on the Schaeffler diagram. *Welding Journal* 66(10): 289-s.

18. Nakao, Y., Nishimoto, K. and Zhang, W. 1988, Effects of rapid solidification by laser surface melting on solidification modes and microstructure of stainless steel , *Trans. JWJI*:19:101.

19. Laursen, B., Olsen, F., Yardy, J., Funder-Kristensen, T. 1997. Experimental determination of the primary solidification phase dependency on the solidification velocity of 17 different stainless steel compositions, Proceedings *ASM International Conference on Welding and Joining Science and Technology*, Madrid Spain, Mar 10-22: 571-580

20. Inoue, H., Koseki, T., Ohkita, S. and Tanaka, T. Effect of solidification and subsequent ferrite-to-austenite massive transformation in an austenitic stainless steel weld metal. *ISIJ* :1248-1257.

21. Pacary, G. Moline, M. and Lippold, J. C. 1990. A diagram for predicting the weld solidification cracking susceptibility of pulsed-laser welds in austenitic stainless steel. *EWI Research Brief* No. B9008, Edison Welding Institute.

22. Lippold, J. C. Solidification behavior and cracking susceptibility of pulsed-laser welds in austenitic stainless steel. *Welding Journal*, 73(6): 129-s to 139-s.

23. Campbell, R. D. and Walsh, D. W. 1993. Weldability testing. *ASM Handbook*, vol 2: 603.

24. Weeter, L.A., Albright, C.E., and Jones, W.H. 1986. Development of a weldability test for pulsed laser beam welds.*Welding Journal,* 65(8): 51-s to 62-s.

25. Suutula, N. , Takalo, T. and Moisio, T. 1979. Relationship between solidification and microstructure in austenitic and austenitic-ferritic stainless steel welds. *Metall. Trans A*, 10A(4): 512-514

26. Brooks, J. A., Yang, N., and Krafcik, J.. 1992. On the Origin of Ferrite Morphologies of Primary Ferrite Solidified Austenitic Stainless Steel Welds. *Recent Trends In Welding Science and Technology*: Eds S. A. David and J. M. Vitek. ASM International, Materials Park: 173-180.

27. Borland, J. C. and Younger, R. N. 1960. Some aspects of cracking in welded Cr-Ni Austenitic steels, *British Welding Journal*, vol.7: 22-59.

28. Brooks, J. A. and Lambert, F. J. Jr. 1978. The effect of phosphorous and sulfur and ferrite content on weld cracking of type 309 stainless steel. *Welding Journal*: 51(5): 139-s.

29. Brooks, J. A. 1975. Weldability of high N, high Mn austenitic stainless steel. *Welding Journal* 54(6): 189-s to 195-s.

30. Li, L. and Messler, R. W., 1999. The effects of phosphorous and sulfur on susceptibility to weld hot crackig in austenitic stainless steels. *Welding Journal* 78(12): 387-s.

31. Kajampaa, V., Suutala, N., Takalo, T., and Moisio, T. 1979. Correlation between solidification cracking and microstructure in austenitic and austenitic-ferritic stainless steel welds. *Welding Research Int.*, 9(2): 55-75.

32. Hee-Sung Ann, Chi-Seung Park, Byung-Chul Kim, Jong-Hyun Park. 1989. Proposal of Solidification Sequences and Microstructure Characterization in Dissimilar Welds. *Recent Trends in Welding Science and Technology.* Eds. S.A. David and J. M. Vitek. ASM International, Metals Park: 257-262.

33. J. W. Elmer, J. Wong and T. Ressler, "Direct observation of phase transformations in austenitic stainless steel welds using in-situ spatially resolved and time resolved x-ray diffraction," The Second International Symposium on the Joining of Advanced Materials ASM Materials Solutions '99, Cincinnati, Ohio, November 1-4, 1999.

34. Schwarzer, R. A . 1997, Automated crystal lattice orientation mapping using a computer controlled SEM, *Micron*,28(3): 249-265.

35. Their, H. 1976. *DVS-Berichte*, Vol. 41. 100-104.

36. Masumoto, I., Tamaki, K.,and Kutsuna, M. 1972. Hot cracking of austenitic stainless steel weld metal, *Trans. JWS*, 41(11): 1306.

37. Arata, J., Matsuda, F., and Katayama, S. 1976. Fundamental investigation on solidification behavior of fully austenitic and duplex structures and effect of ferrite on microsegregation. *Trans. JWRI*, 5(2): 35.

38. Lippold, J. C. 1982. Weld cracking mechanism in austenitic stainless steels. *Trends in Welding Research in the U.S.*, ASM conference proceedings, Metals Park, Ohio, 209-247.

39. Brooks, J. A., Thompson, A. W., and Williams, J. C. 1983. Variations in weld ferrite content due to P and S. *Welding Journal* , 72(8): 220-s to 225-s.

40. Matsuda, F., Nakagawa, H., Uehara, T., Kaatayama, S., Arata, Y. 1979. A new explanation for role of delta-ferrite improving solidification crack susceptibility in austenitic stainless steel. *Journal JWRI*, 8(1), p105-112.

41. Hull, F. C. 1967. Effect of delta ferrite on hot cracking of stainless steel. *Welding Journal*, 46(9); 399-s to 409-s.

Table 1 Alloy Compositions and Calculated Cr_{eq}/Ni_{eq} Ratios

Heat # /Element wt.%	1	2	3	4	5	6	7	8	9	10
C	0.03	0.03	0.03	0.03	0.03	0.03	0.03	0.03	0.03	0.03
Mn	1.48	1.49	1.48	1.49	1.48	1.48	1.47	1.48	1.49	1.47
Si	0.62	0.59	0.62	0.61	0.57	0.57	0.59	0.61	0.59	0.61
P	0.03	0.03	0.03	0.03	0.03	0.03	0.03	0.03	0.03	0.03
S	0.04	0.04	0.04	0.11	0.27	0.42	0.11	0.12	0.27	0.18
Cr	17.55	19.18	18.37	18.45	18.47	18.45	16.87	17.78	17.77	18.16
Ni	10.51	8.92	9.73	8.60	8.49	8.61	10.08	9.29	9.30	8.83
Mo	0.35	0.35	0.35	0.35	0.35	0.35	0.35	0.35	0.35	0.35
Cu	0.31	0.30	0.30	0.30	0.30	0.30	0.30	0.31	0.30	0.30
N	0.02	0.02	0.02	0.02	0.02	0.02	0.02	0.02	0.02	0.02
Creq/Nieq WRC92	1.48	1.89	1.67	1.85	1.87	1.85	1.48	1.67	1.67	1.78
Creq/Nieq H & S	1.55	1.95	1.73	1.92	1.94	1.92	1.55	1.74	1.74	1.85

Table 2. Maximum Crack Length (mm)

Heat# (%) Strain	1	2	3	4	5	6	7	8	9	10
0.5		5								
1.0	0	15	0	0	0	0	13	8	0	0
2.5	10	15	0	11	0	10	11	13	0	0
3.6	13	18	8	15	0	15	15	8	15	0

List of Figures

Figure 1. Varestraint results showing total crack length vs. augmented strain.

Figure 2. (a) Solidification and cracking behavior of Heat 7 containing 0.011% S with a $\mathrm{Cr_{eq}/Ni_{eq}}$ ratio of 1.55, dark etching regions solidified as primary austenite, lighter regions as primary ferrite. (b) higher magnification showing cracks in region of primary austenite solidification.

Figure 3. (a) Solidification and cracking behavior of Heat 1 containing 0.011% S with a $\mathrm{Cr_{eq}/Ni_{eq}}$ ratio of 1.55, (b) higher magnification showing primary ferrite solidified structure except in region of crack where final solidification occurred as austenite. (c) SEM image showing Mn and Cr containing sulfides with some eutectic ferrite in cell boundaries.

Figure 4. Heat 10 $\mathrm{Cr_{eq}/Ni_{eq}} = 1.85$ tested at 1% strain (a) primary ferrite solidified structure exhibiting both skeletal and lathy ferrite morphologies characteristic of alloys with $\mathrm{Cr_{eq}/Ni_{eq}}$ ratios of 1.73-1.85. Note evidence of high strain in grain boundary regions resulting from Varestraint test (b) SEM image showing large sulfide particles at solidification grain boundary (A), ferrite/austenite interface (B), and cell boundaries (C).

Figure 5. Microstructure of Heat 2 typical of GTA welds in heats with $\mathrm{Cr_{eq}/Ni_{eq}}$ ratios of 1.92 – 1.95. Sample tested at 2.5% strain exhibiting a crack and a lathy ferrite morphology. (b) higher magnification showing sulfides in grain boundary region.

Figure 6. Plot of laser weld cracking behavior.

Figure 7. (a) Laser weld of Heat 7 with a S content of 0.11% and a $\mathrm{Cr_{eq}/Ni_{eq}}$ ratio of 1.55, (b) higher magnification of (a) showing distinct cellular appearing primary austenite solidification structure and intergranular nature of cracks.

Figure 8. STEM image of laser weld in Heat 7 with a S content of 0.04% and a $\mathrm{Cr_{eq}/Ni_{eq}}$ ratio of 1.55 showing Al containing oxides "O" and Cr containing phosphides "P".

Figure 9. Position tagged spectroscopy results for laser weld in Heat 7 showing (a) region of crack, and (b) phosphorous map and (c) sulfur map. Constituent associated with crack is enriched in both elements.

Figure 10. (a) Microstructure of laser weld in Heat 9 with a S content of 0.27% and a $\mathrm{Cr_{eq}/Ni_{eq}}$ ratio of 1.74. (b) higher magnification of (a) showing small cracks in the primary austenite solidified structure.

Figure 11 (a) Microstructure of laser weld in Heat 3 with a S content of 0.04% and a $\mathrm{Cr_{eq}/Ni_{eq}}$ ratio of 1.74 showing the nature of mixed mode solidification with austenite solidification (dark etching grains) generally confined to region of pulse weld boundaries. (b) Higher magnification of (a) taken in region of weld overlap.

Figure 12. (a) Microstructure of laser weld in Heat 2, $\mathrm{Cr_{eq}/Ni_{eq}} = 195$, 0.04% S, (b) higher magnification of boundary regions showing primary ferrite solidified structure.

Figure 13. (a) Microstructure of laser weld in Heat 6with $\mathrm{Cr_{eq}/Ni_{eq}} = 1.92$ and 0.42% S, (b) boundary regions showing primary ferrite solidified structure containing high concentration of sulfides, globular sulfides at HAZ boundary and sulfide and ferrite

stringers in base material. (c) TEM micrograph showing globular sulfides in solidification boundary, spherical Mn and Cr containing sulfides nucleated at amorphous aluminum oxide particles, and fine uniformly distributed sulfides.

Figure 14. SEM micrograph with BEKP patterns showing epitaxial solidification of austenite at interpulse boundary. The BEKP patterns show that both regions have same austenite orientation. (Heat 3)

Figure 15. SEM micrograph showing cellular structure growing a short distance from the base material and changing to apparent featureless ferrite solidification. BEKP patterns showing epitaxial solidification of austenite form base material with same orientations, but orientation of ferrite solidification different. (Heat 3)

Figure 16. SEM micrograph with BEKP patterns showing solidification as ferrite form base grain. The same BEKP patterns show different austenite orientations for the two regions. (Heat 3)

Figure 17. (a) SEM micrograph with (b) corresponding orientation imaging map of primary austenite solidified laser weld of Heat 1. Note fusion zone boundary in map is not apparent due to epitaxial growth.

Figure 18. (a) SEM micrograph with (b) corresponding orientation imaging map of primary ferrite solidified laser weld of Heat 2. Note fusion zone boundary in map is more apparent than in Figure 17 due to the orientations across the fusion zone boundary.

Figure 19. Summary of GTA weld results showing region of good solidification cracking resistance.

Figure 20. Combined results of both GTA and pulsed laser welds showing a region of good weldability limited by LBW at low Cr_{eq}/Ni_{eq} ratios and by GTA at high ratios.

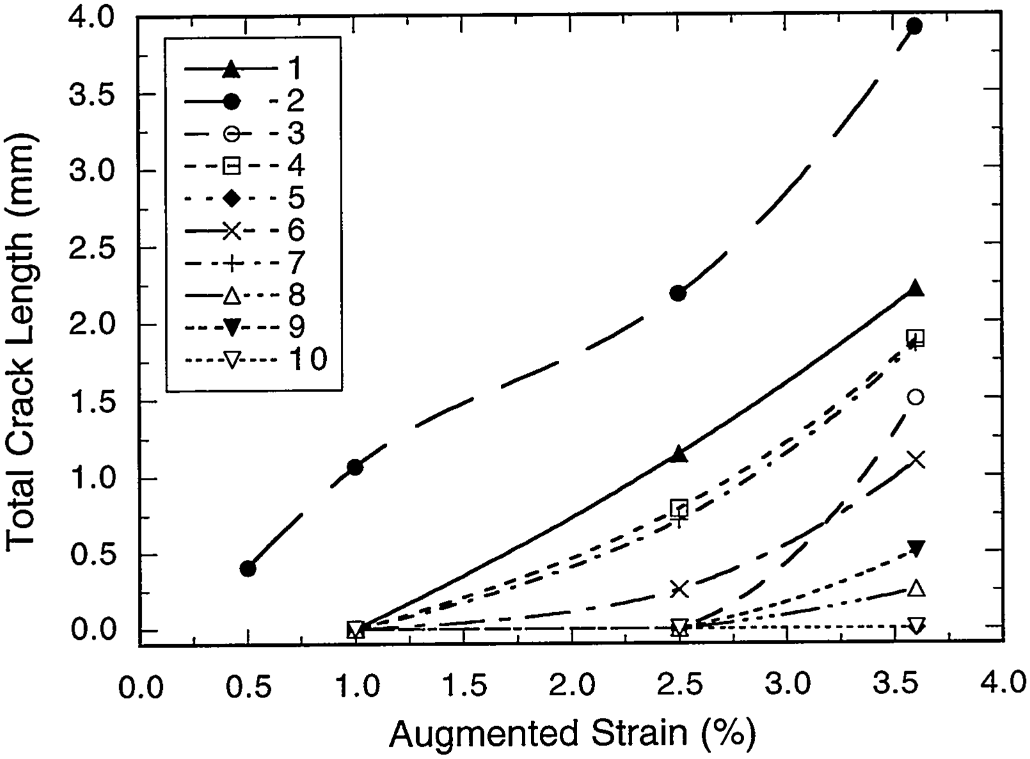

Figure 1. Varestraint results showing total crack length vs. augmented strain.

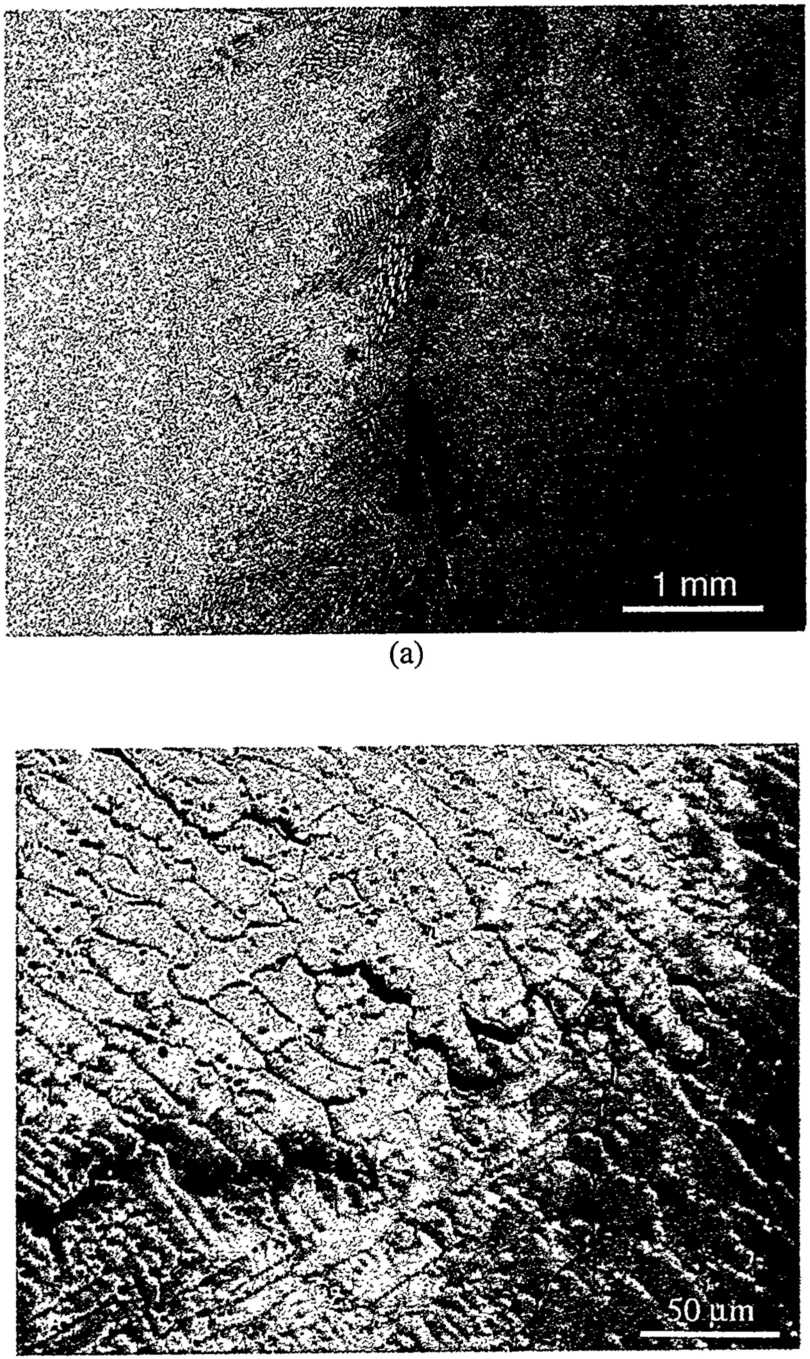

(a)

(b)

Figure 2. (a) Solidification and cracking behavior of Heat 7 containing 0.011% S with a Cr_{eq}/Ni_{eq} ratio of 1.55, dark etching regions solidified as primary austenite, lighter regions as primary ferrite. (b) higher magnification showing cracks in region of primary austenite solidification.

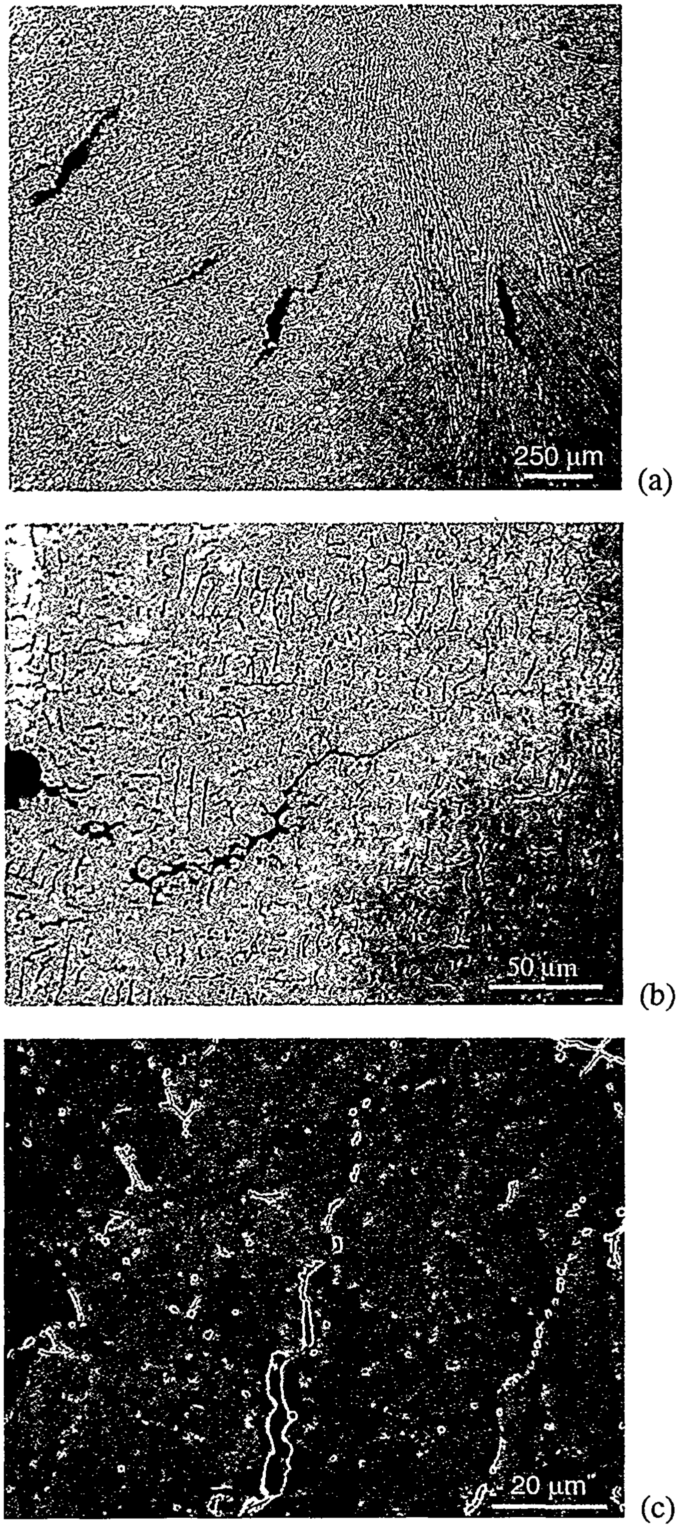

Figure 3. (a) Solidification and cracking behavior of Heat 1 containing 0.011% S with a Cr_{eq}/Ni_{eq} ratio of 1.55, (b) higher magnification showing primary ferrite solidified structure except in region of crack where final solidification occurred as austenite. (c) SEM image showing Mn and Cr containing sulfides with some eutectic ferrite in cell boundaries.

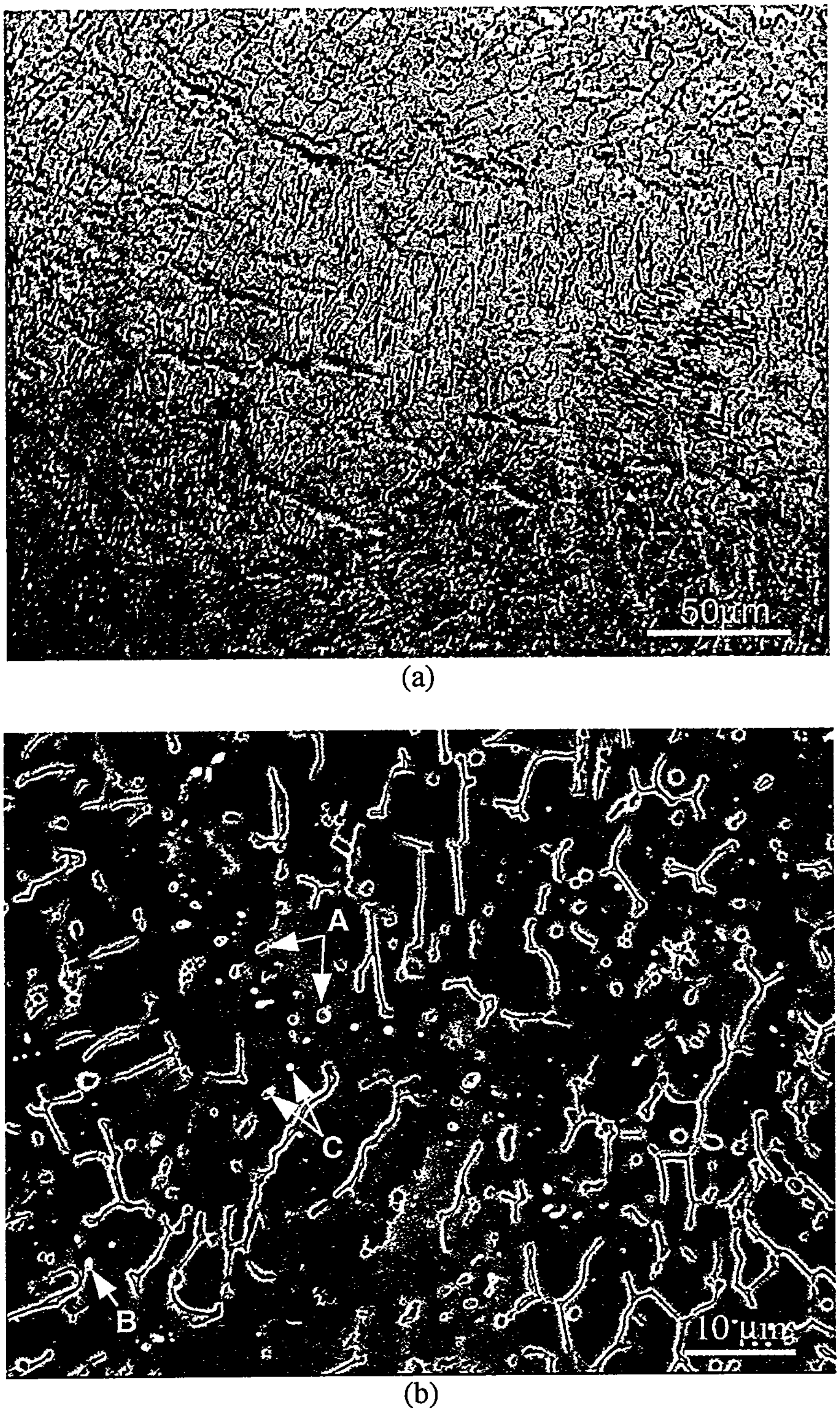

(a)

(b)

Figure 4. Heat 10 $Cr_{eq}/Ni_{eq} = 1.85$ tested at 1% strain (a) primary ferrite solidified structure exhibiting both skeletal and lathy ferrite morphologies characteristic of alloys with Cr_{eq}/Ni_{eq} ratios of 1.73-1.85. Note evidence of high strain in grain boundary regions resulting from Varestraint test (b) SEM image showing large sulfide particles at solidification grain boundary (A), ferrite/austenite interface (B), and cell boundaries (C).

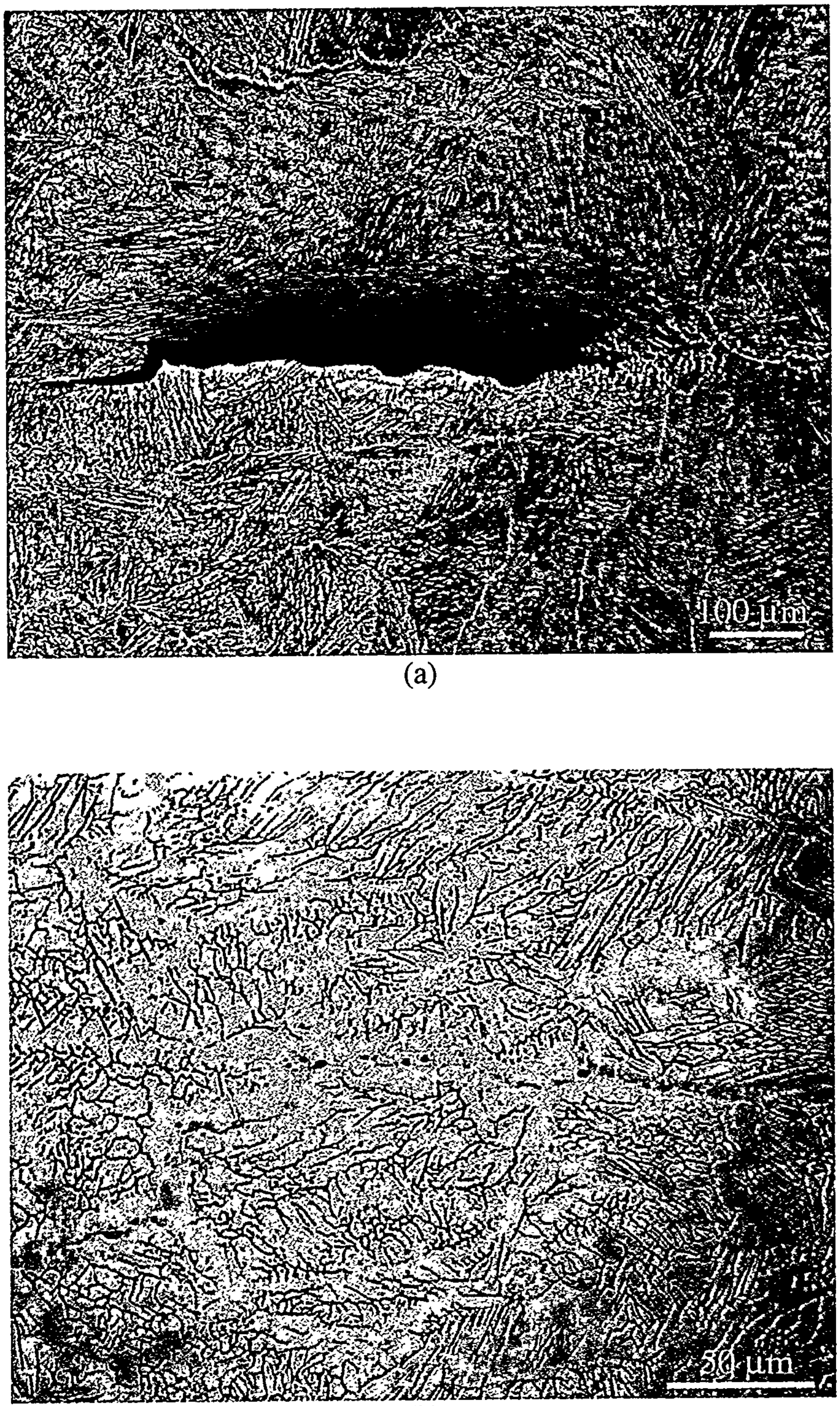

(a)

(b)

Figure 5. Microstructure of Heat 2 typical of GTA welds in heats with Cr_{eq}/Ni_{eq} ratios of 1.92 – 1.95. Sample tested at 2.5% strain exhibiting a crack and a lathy ferrite morphology. (b) higher magnification showing sulfides in grain boundary region.

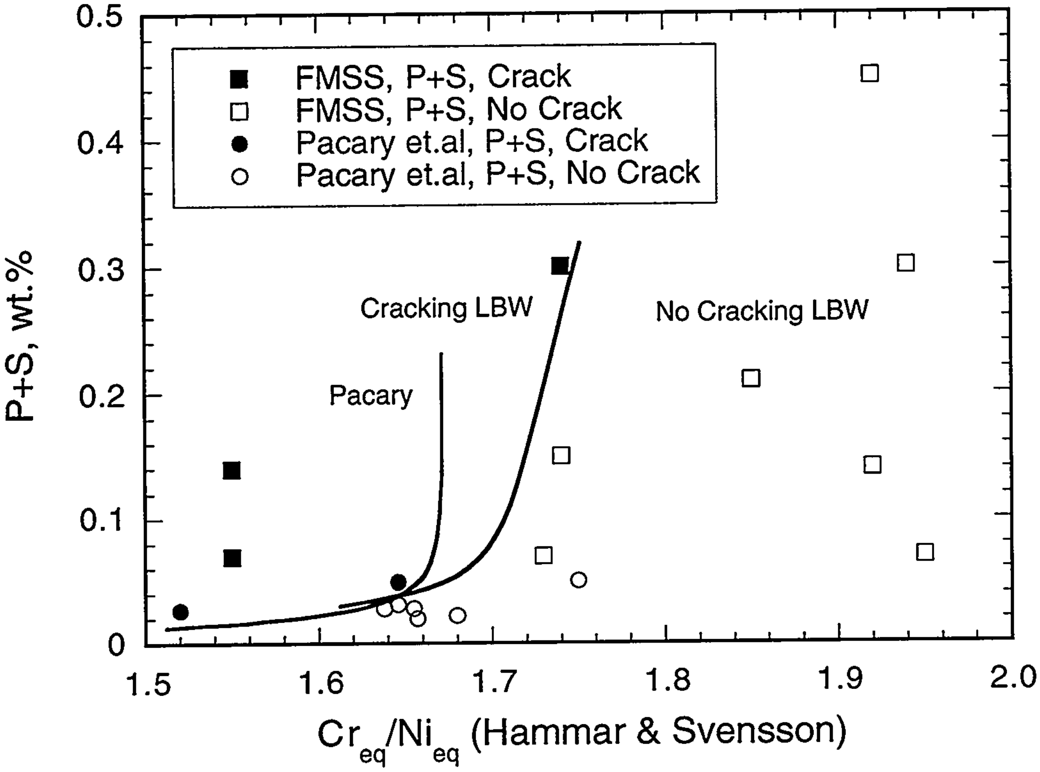

Figure 6. Plot of laser weld cracking behavior.

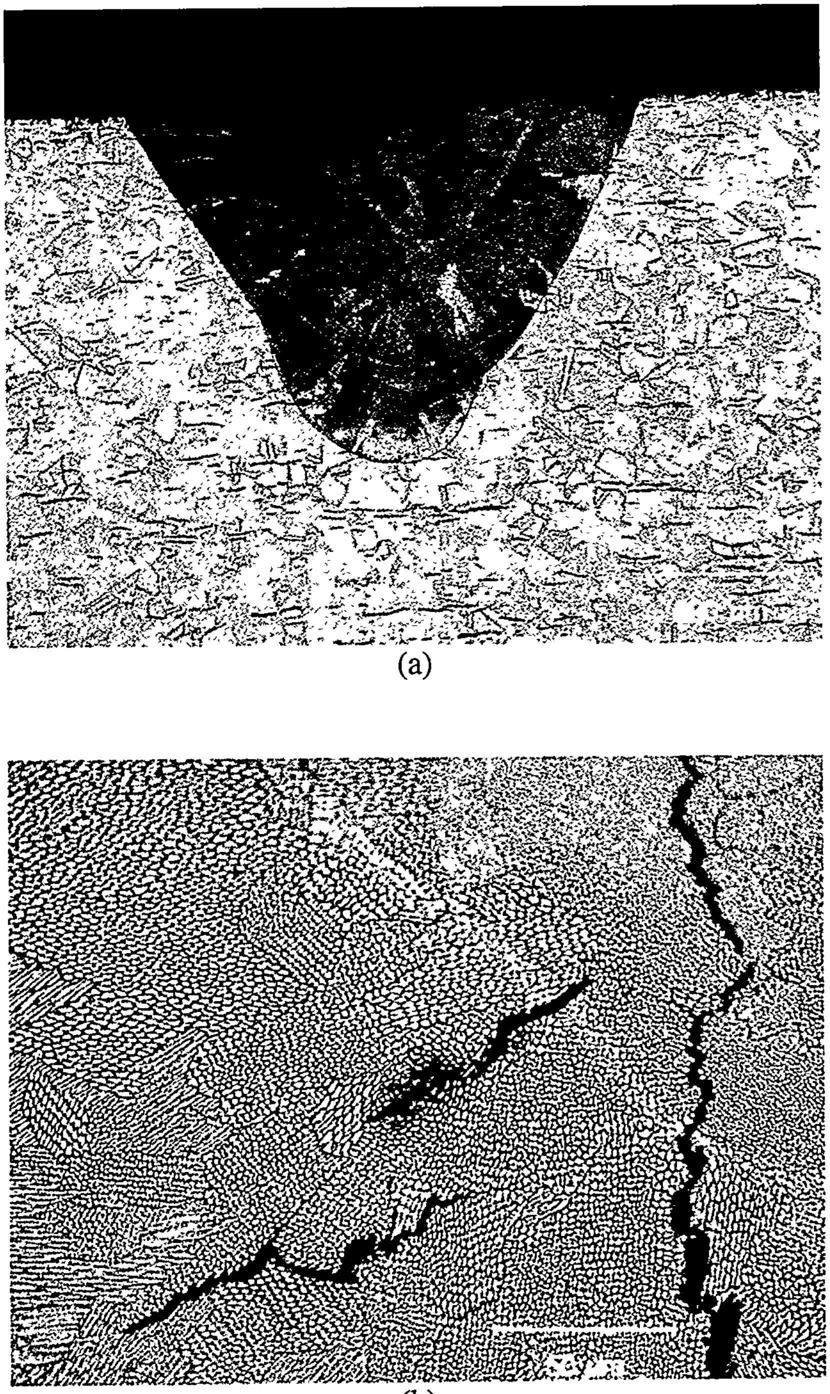
(a)

(b)

Figure 7. (a) Laser weld of Heat 7 with a S content of 0.11% and a Cr_{eq}/Ni_{eq} ratio of 1.55, (b) higher magnification of (a) showing distinct cellular appearing primary austenite solidification structure and intergranular nature of cracks.

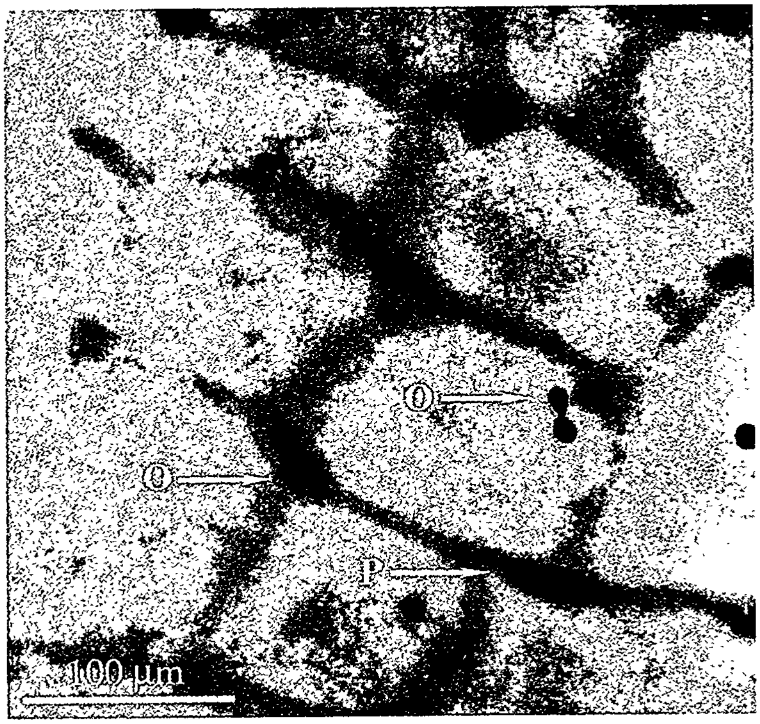

Figure 8. STEM image of laser weld in Heat 7 with a S content of 0.04% and a Cr_{eq}/Ni_{eq} ratio of 1.55 showing Al containing oxides "O" and Cr containing phosphides "P".

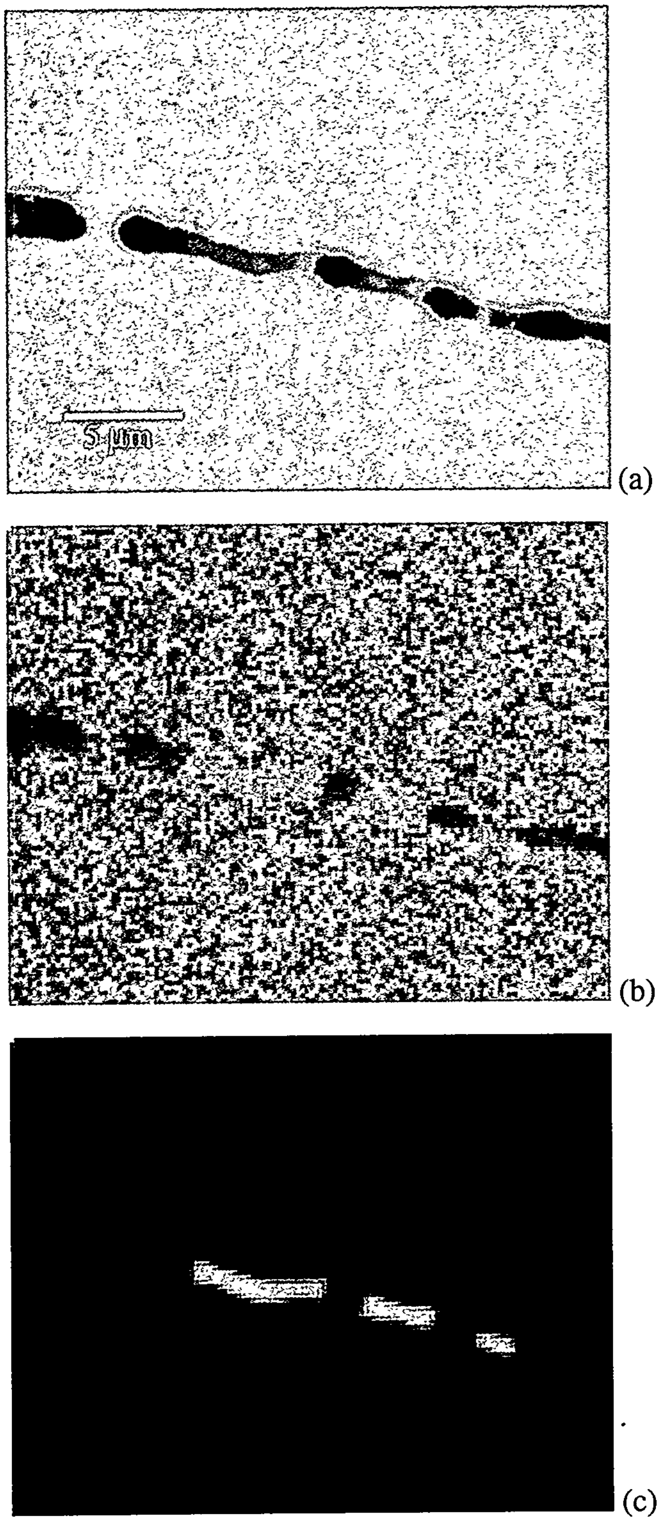

Figure 9. Position tagged spectroscopy results for laser weld in Heat 7 showing (a) region of crack, and (b) phosphorous map and (c) sulfur map. Constituent associated with crack is enriched in both elements.

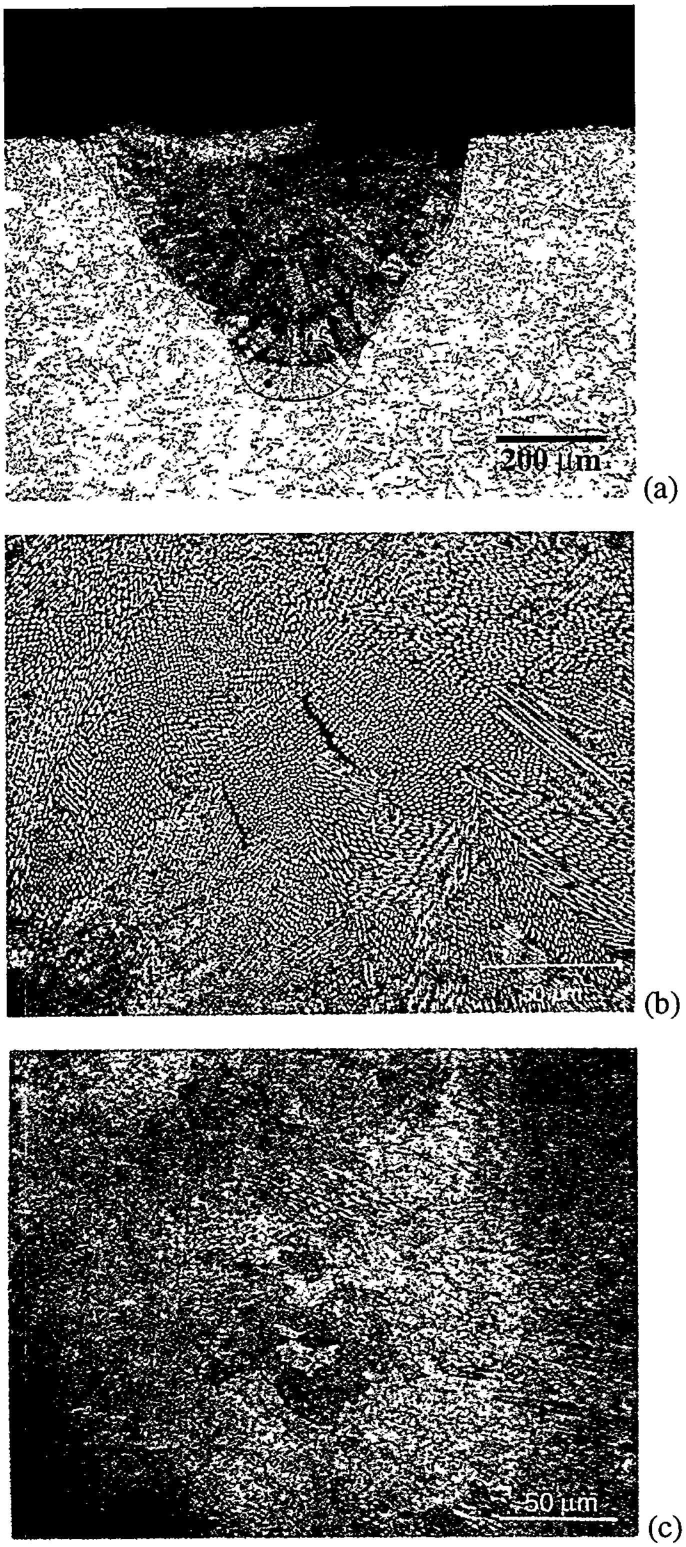

Figure 10. (a) Microstructure of laser weld in Heat 9 with a S content of 0.27% and a Cr_{eq}/Ni_{eq} ratio of 1.74. (b) higher magnification of (a) showing small cracks in the primary austenite solidified structure.

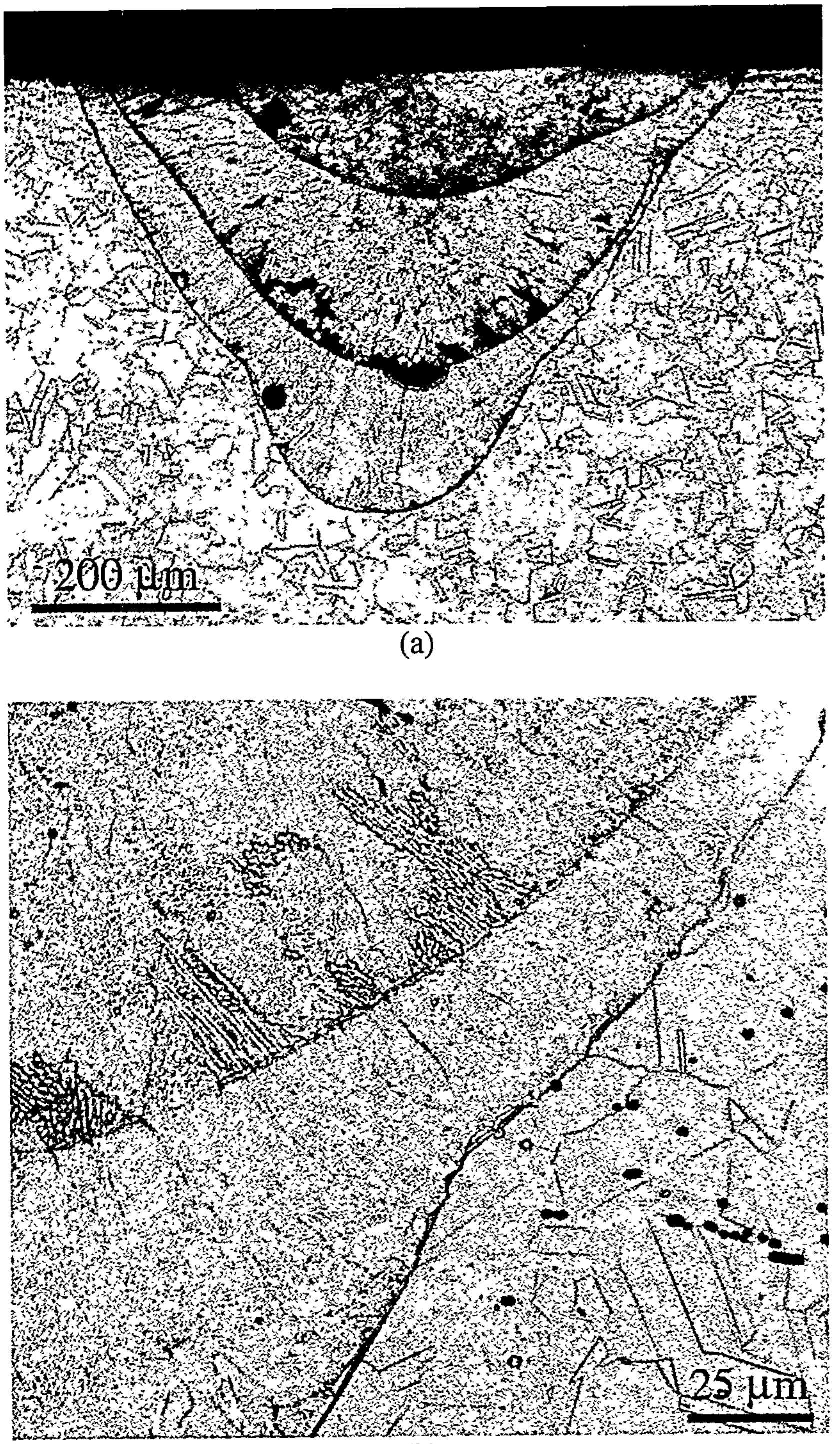

(a)

(b)

Figure 11 (a) Microstructure of laser weld in Heat 3 with a S content of 0.04% and a Cr_{eq}/Ni_{eq} ratio of 1.74 showing the nature of mixed mode solidification with austenite solidification (dark etching grains) generally confined to region of pulse weld boundaries. (b) Higher magnification of (a) taken in region of weld overlap.

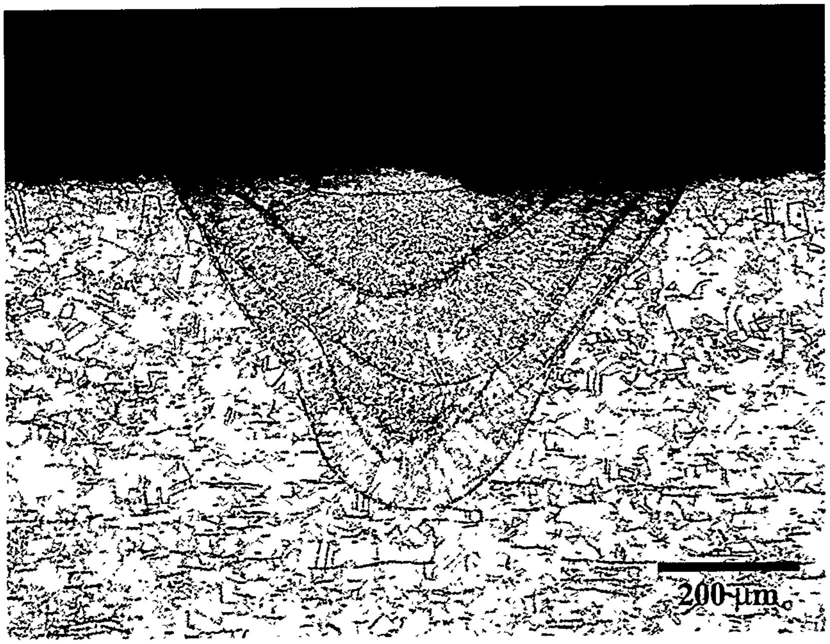

(a)

(b)

Figure 12. (a) Microstructure of laser weld in Heat 2, $Cr_{eq}/Ni_{eq} = 195$, 0.04% S, (b) higher magnification of boundary regions showing primary ferrite solidified structure.

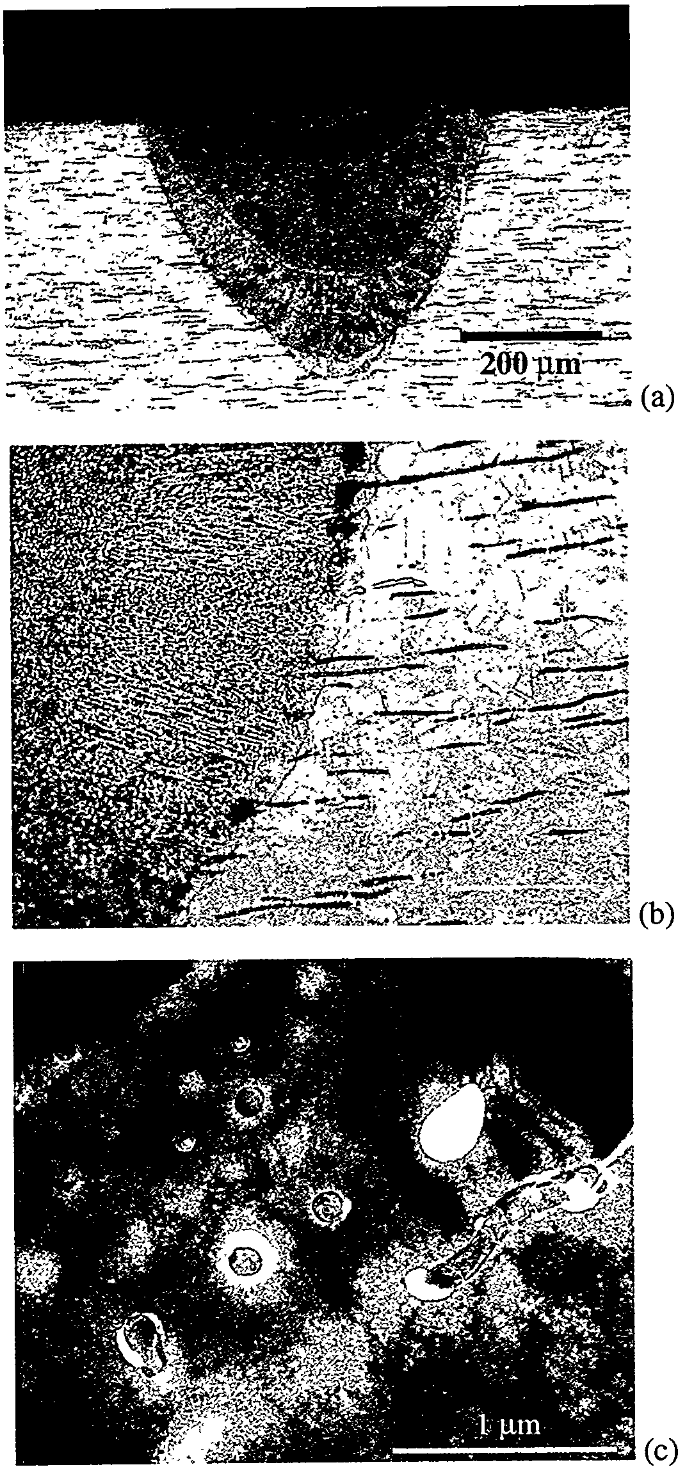

Figure 13. (a) Microstructure of laser weld in Heat 6with $Cr_{eq}/Ni_{eq} = 1.92$ and 0.42% S, (b) boundary regions showing primary ferrite solidified structure containing high concentration of sulfides, globular sulfides at HAZ boundary and sulfide and ferrite stringers in base material. (c) TEM micrograph showing globular sulfides in solidification boundary, spherical Mn and Cr containing sulfides nucleated at amorphous aluminum oxide particles, and fine uniformly distributed sulfides.

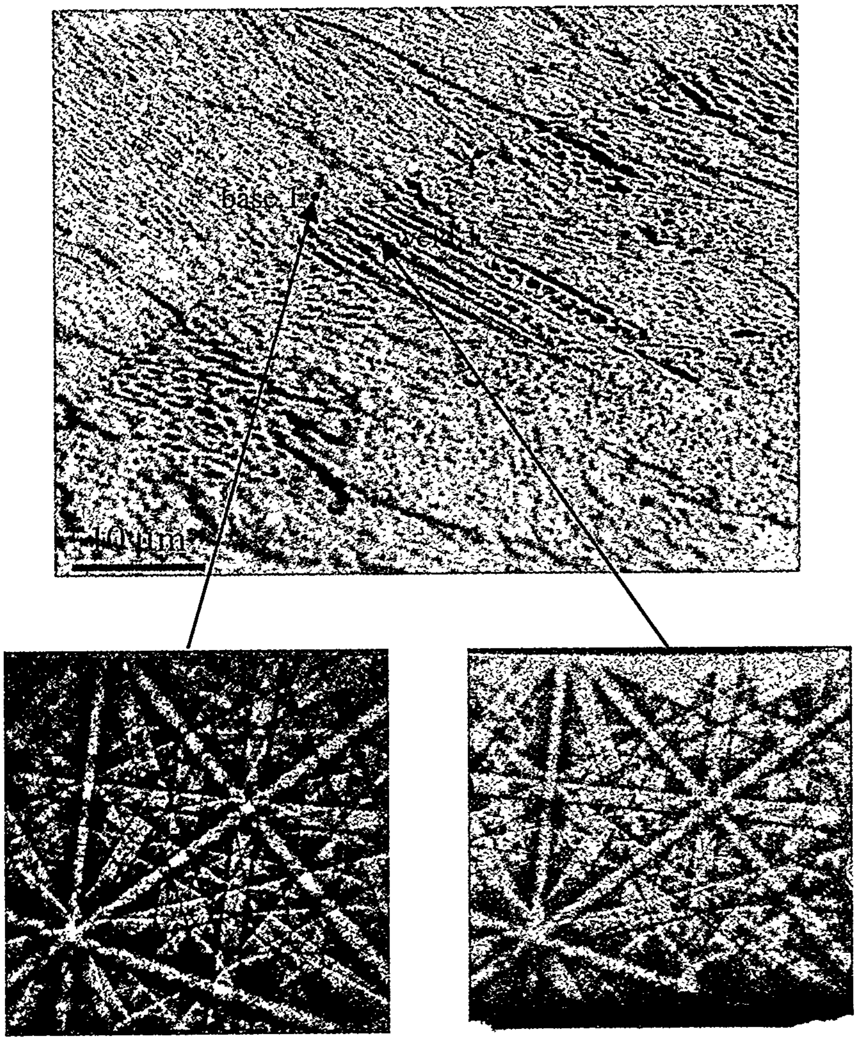

Figure 14. SEM micrograph with BEKP patterns showing epitaxial solidification of austenite at interpulse boundary. The BEKP patterns show that both regions have same austenite orientation. (Heat 3)

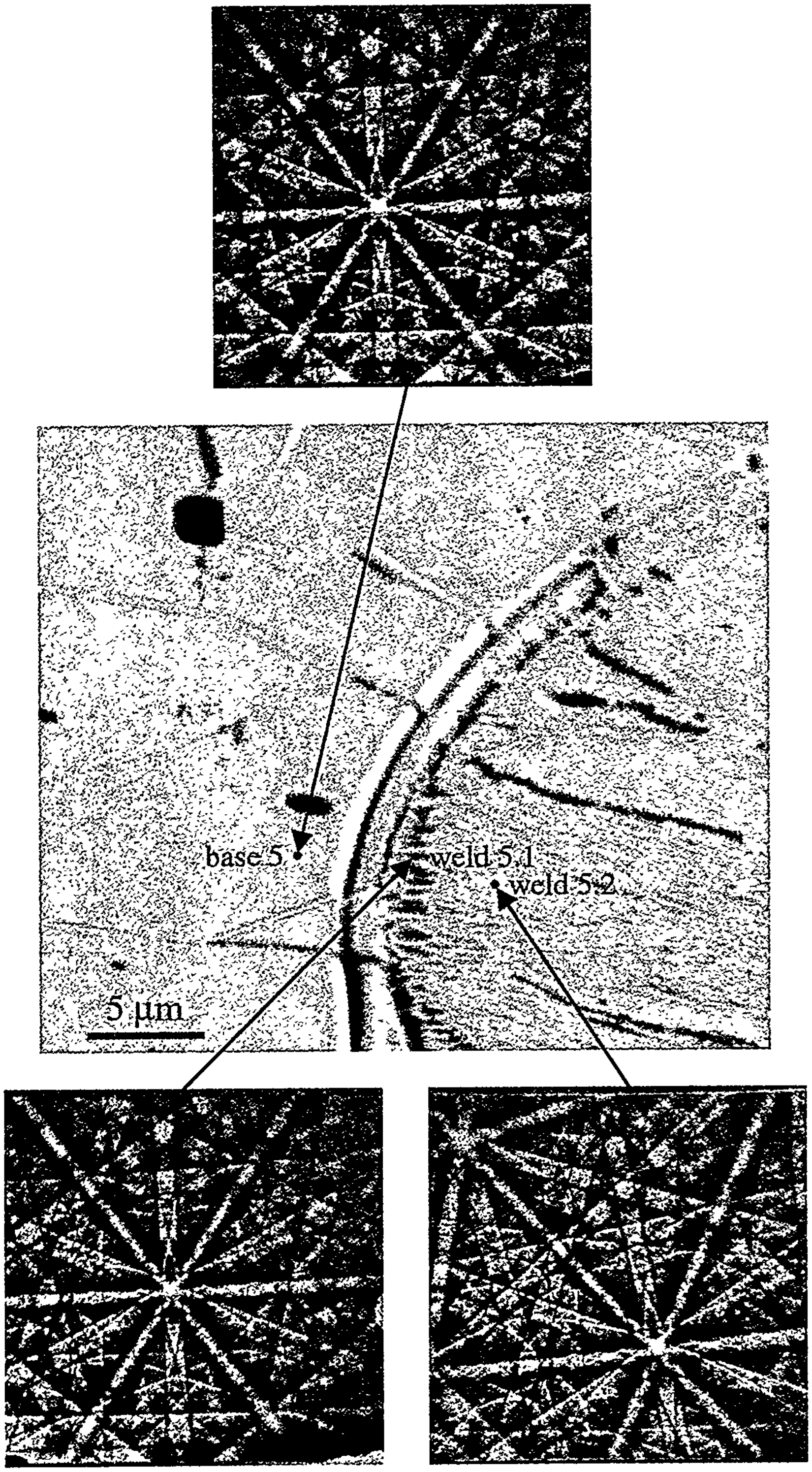

Figure 15. SEM micrograph showing cellular structure growing a short distance from the base material and changing to apparent featureless ferrite solidification. BEKP patterns showing epitaxial solidification of austenite form base material with same orientations, but orientation of ferrite solidification different. (Heat 3)

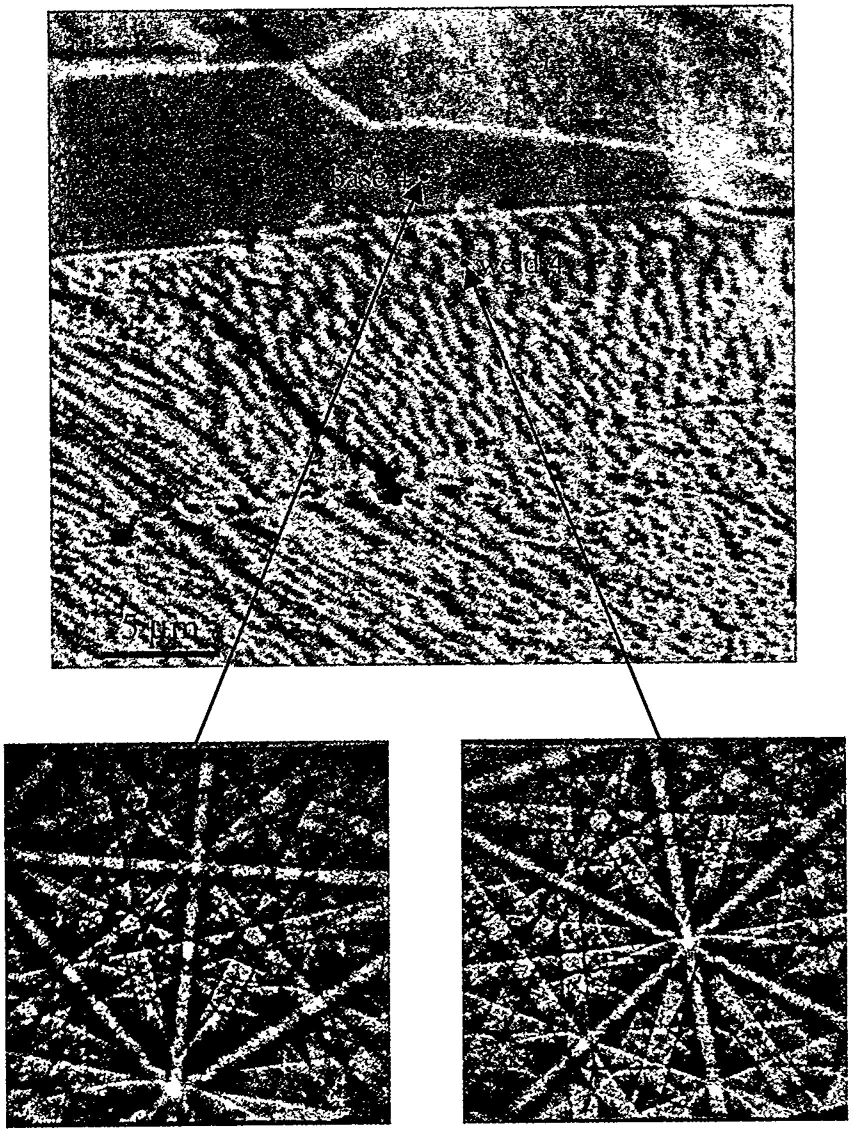

Figure 16. SEM micrograph with BEKP patterns showing solidification as ferrite form base grain. The same BEKP patterns show different austenite orientations for the two regions. (Heat 3)

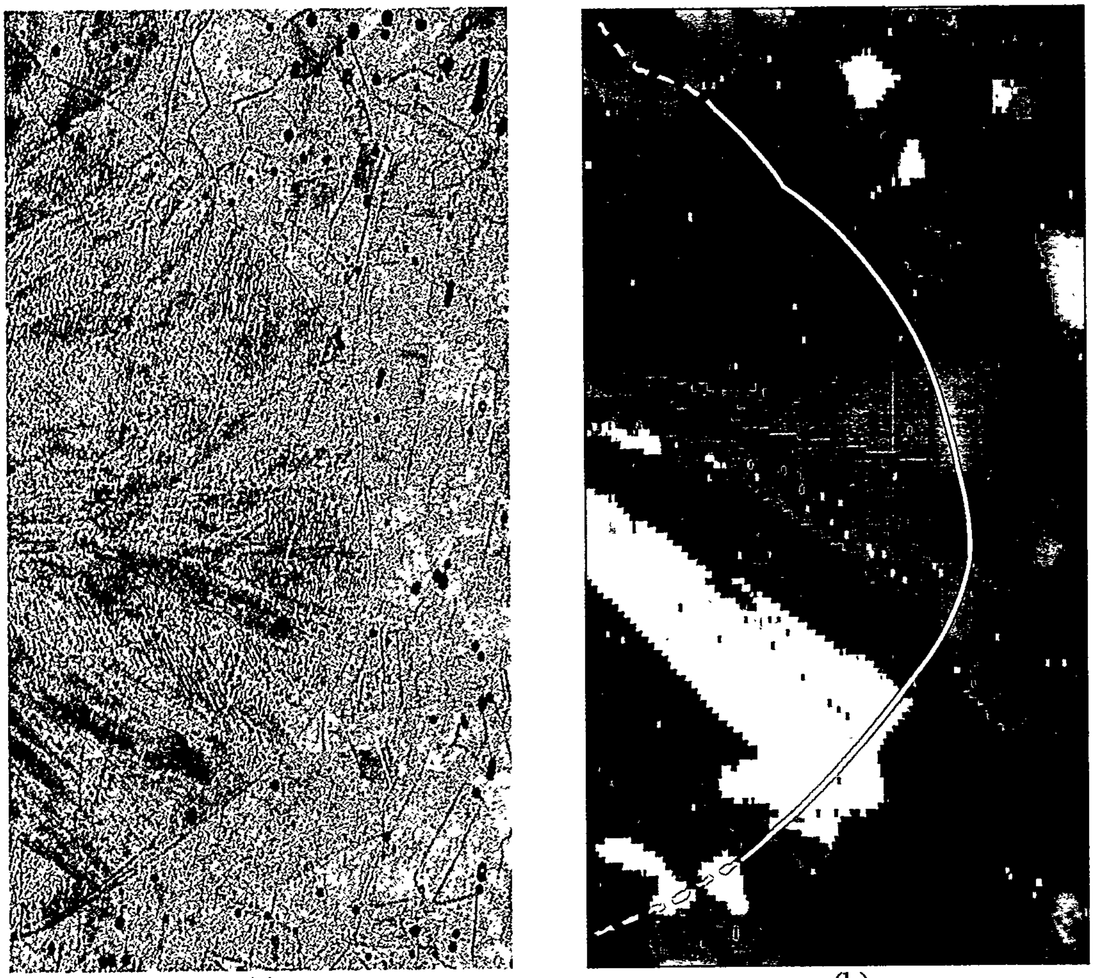

(a) (b)

Figure 17. (a) SEM micrograph with (b) corresponding orientation imaging map of primary austenite solidified laser weld of Heat 1. Note fusion zone boundary in map is not apparent due to epitaxial growth.

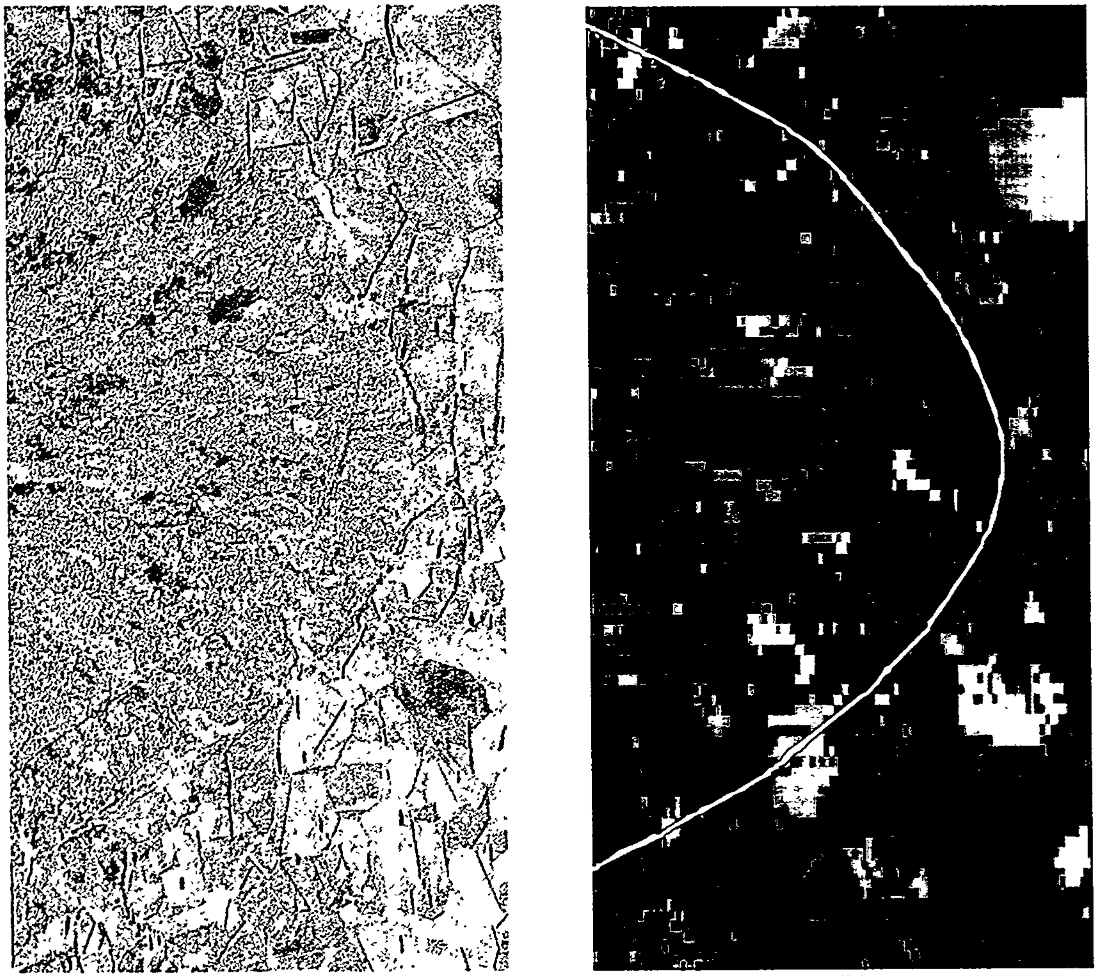
(a) (b)

Figure 18. (a) SEM micrograph with (b) corresponding orientation imaging map of primary ferrite solidified laser weld of Heat 2. Note fusion zone boundary in map is more apparent than in Figure 17 due to the orientations across the fusion zone boundary.

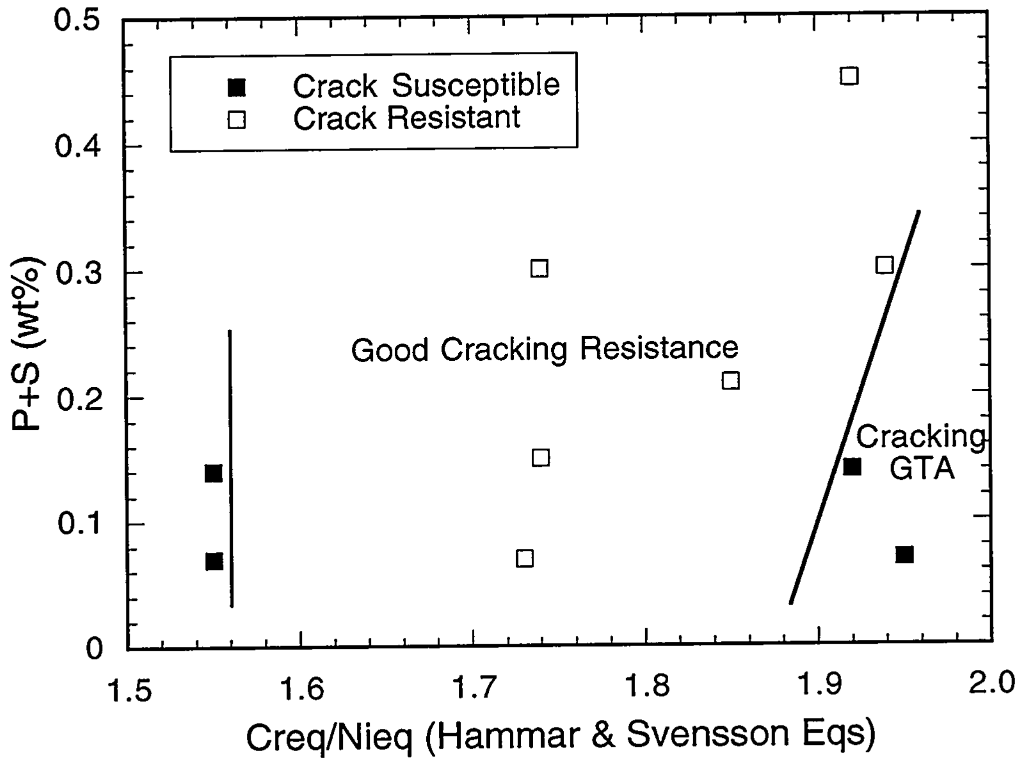

Figure 19. Summary of GTA weld results showing region of good solidification cracking resistance.

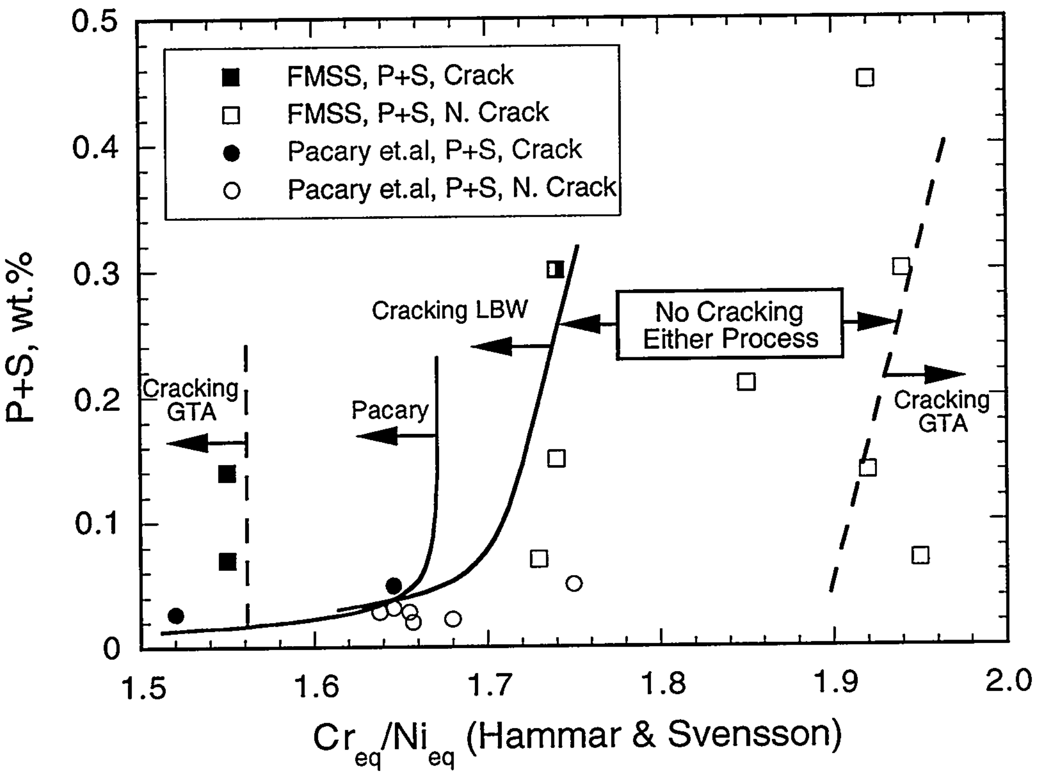

Figure 20. Combined results of both GTA and pulsed laser welds showing a region of good weldability limited by LBW at low Cr_{eq}/Ni_{eq} ratios and by GTA at high ratios.